Polymer / Transparent Electrode Interface Studies with Applications for Organic Solar Cells

Kristina Marie Knesting

A dissertation

submitted in partial fulfillment of the

requirements for the degree of

Doctor of Philosophy

University of Washington

2013

Reading Committee:

David S. Ginger, Chair

Charles T. Campbell

Munira Khalil

Program Authorized to Offer Degree:

Chemistry

University of Washington

Abstract

Polymer / Transparent Electrode Interface Studies with Applications for Organic Solar Cells

Kristina Marie Knesting

Chair of the Supervisory Committee:
Professor David S. Ginger
Department of Chemistry

The field of organic photovoltaics continues to progress through a combination of improved materials selection and a deeper understanding of operational mechanisms. We contribute to advances in both areas through study of the interface between the semiconducting polymer and the transparent electrode. This interface is the site of charge injection and extraction, and this thesis specifically focuses upon nanoscale modification of interfacial properties resulting in measurable changes in bulk device performance and ultimately leading to a deepened understanding of device operation.

The polymer / transparent electrode interface is modified through use of phosphonic acid self-assembled monolayers (PA SAMs). Using micro-contact printing, we deposit PA SAMs and spatially modulate the work function of the transparent conductive oxide, indium tin oxide (ITO). The contact potential difference on and off the SAM shows strong contrast and high resolution despite only sub-nanometer variations in topography. We incorporate the patterned

ITO into a light-emitting diode as a way to visually confirm changes in charge injection resulting from changes in ITO work function. The patterned electroluminescence is stronger in regions where the SAM is present, indicating locally improved charge injection.

We also use monolayers of PA SAMs (on the order of ~1nm thick) to modify the work function of the hole-extracting contact, ITO, in polymer/fullerene bulk heterojunction solar cells. We observe a linear dependence of the open-circuit voltage of these organic photovoltaic devices on the modified ITO work function when using a donor polymer with a deep-lying highest-occupied molecular orbital (HOMO). We measure charge carrier lifetimes using transient photovoltage and charge extraction in a series of SAM-modified devices. As expected, these measurements show systematically longer carrier lifetimes in devices with higher open-circuit voltages; however, the trends provide useful distinctions between different hypotheses of how transient photovoltage decays might be controlled by surface chemistry. We interpret our results as being consistent with changes in band-bending at the ITO/bulk heterojunction interface which have the net result of altering the internal electric field to help prevent electrons in fullerene domains from recombining at the hole-extracting electrode.

Table of Contents

List of Figures

List of Tables

Acknowledgements

I would like to thank the Department of Energy (DOE) for supporting me, both through opportunities as an undergraduate in the Summer School in Nuclear and Radiochemistry, and also as a graduate student through the Office of Science Graduate Fellowship and DOE-funded Energy Frontier Research Center (EFRC) (Center for Interface Science: Solar Electric Materials) collaborations. These awards and opportunities have enabled me to develop tremendously as a scientist, and as a better-rounded person. I would be remiss if I failed to acknowledge the many wonderful opportunities I have had as a result of participation in the EFRC throughout most of my time in graduate school. Not only was I able to meet many of our wonderful collaborators face-to-face, but I also had the chance to work side-by-side with them at national labs. It was a fantastic (albeit brief) experience working at the National Renewable Energy Lab with our EFRC collaborator Dr. Dana Olson and his group. The EFRC collaboration also provided the materials that are the crux of this thesis, so to Prof. Seth Marder and his group at Georgia Institute of Technology, I paraphrase Bob Hope: "Thanks, for the molecules!"

At the University of Washington, special thanks also go out to Roy Olund, Lon Buck, and the Chemistry Electronics shop for building the "black box" circuitry of our transient photovoltage and charge extraction experiment, as well as to Dr. Raj Giridharagopal, former Ginger Lab post-doc, for building the LED driver box. Many other members of the Ginger Lab, past and present, have been an integral part of my graduate school training. Glennis Rayermann was amazingly patient and obliging while teaching me programming in Igor Pro, and Dr. Jennifer Chen was incredibly helpful with LabView programming. Drs. Cody Schlenker, Deanna Rodovsky, and Chris Groves were all instrumental in my development as a scientist, and

I would not have made it to this point without my triad of support, both personally and academically, throughout my time in graduate school. Thank you so much; your faith in me means a lot.

Lastly, I thank my research advisor, Prof. David Ginger. To whom much is given, much is expected, and I appreciate your resolute high standards as you sought to maximize my potential as a scientist. Thank you for providing me with a wealth of opportunities and experiences throughout my time in graduate school.

Dedication

To my parents, Ed and Mickey Knesting.

1 Introduction

1.1 Motivation and background

Organic photovoltaics (OPVs) have potential to become a large-scale, printable, low-cost renewable energy source. These devices typically utilize solution-processable semiconducting polymers that can be printed on flexible substrates in a low-cost, "roll-to-roll" style to form films on the order of ~100 nm thick. However, the power conversion efficiency, which is the ratio of electrical power produced to the incoming solar power, is around 10-11% for lab-scale devices.[1,2] Unfortunately, efficiency decreases as the cell areas increase, and thus large-scale OPVs have not yet been able to achieve the same efficiencies.[3] Furthermore, the cost-per-Watt of installed residential photovoltaics in the US is substantial, at best just under a median low of $\$5.00/W_{DC}$ in 2011.[4] With growing energy demands and the desire for low-cost applications[5] both on and off-grid,[6] there is still much interest and attention on improving efficiencies and performance.

With the many components of an OPV, there are multiple approaches that have led to rapid improvements in efficiency. This thesis will focus upon the use of tailored surface chemistries that can control charge injection and extraction, as well as increase cell voltages, in an effort to decrease cost-per-Watt and making OPVs more cost-competitive and feasible for mass production. As one can imagine, there are many ongoing efforts to improve OPV efficiencies, but before we look at ways to improve efficiency, let us first examine the development of a typical device configuration.

1.2 Brief history and basics of OPV architecture and operation

The common OPV configuration of today stems from a few key developments as the mechanistic understanding of these devices improved over the years. Use of organics as the active material in photovoltaic devices was prevalent even in the 1950s, when single material photovoltaic devices typically using small molecules such as anthracene were studied.[6,7] When light is absorbed into an organic, excitons, or electrically neutral quasi-particles, are formed due to the small dielectric constant (typically <4). The electric field created by the sandwich of organic between two different metal electrodes is not sufficiently strong to separate excitons, and thus the single-layer "homo-junction" OPVs suffered from low photovoltages and efficiencies.[6] A major advancement in the field was the development of a bilayer OPV, which is credited to Tang.[8] In this new "heterojunction" configuration, one organic layer acts primarily as a hole-transporting layer (also referred to as electron-donating or "donor" material), while the other organic layer is electron-transporting (also referred to as electron-accepting or "acceptor" material). The presence of a donor/acceptor interface in the organic layer of the device greatly improved exciton dissociation and thereby cell performance.

Naturally, the next significant OPV development increased the donor/acceptor interfacial volume through the advent of the bulk heterojunction (BHJ) that appeared in the literature in 1995.[9-11] The BHJ, or blend of donor/acceptor materials, enabled significant improvements in device efficiencies over the past almost two decades. A significant portion of this thesis focuses on BHJ OPVs, and thus a cartoon of a typical device cross-section and architecture is shown in Figure 1.1. A transparent electrode, most commonly indium tin oxide (ITO), allows light into the cell. The light-absorbing active layer is typically comprised of a blend of an electron donor

(typically a semiconducting polymer) and an electron acceptor material (typically a fullerene-derivative). Commonly, this BHJ is formed by co-dissolving the donor and acceptor into a solution that phase-separates into donor-rich and acceptor-rich regions upon thin film formation. The exciton must diffuse to a donor-acceptor interface prior to relaxation in order for charge separation to occur. If these photo-generated charges avoid recombination, they can diffuse and drift to their respective electrodes,[12] where they are extracted as useful photocurrent.

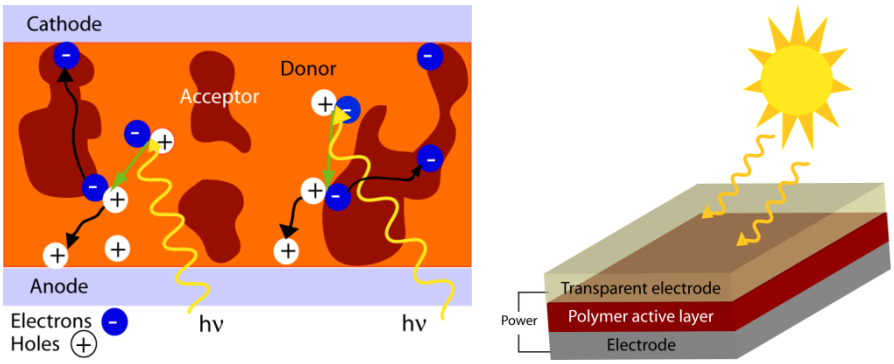

Figure 1.1 Schematic of typical bulk heterojunction OPV cross-section and device stack. Cartoon of typical bulk heterojunction OPV cross-section (left) and device stack (right), not to scale. (Left) As sunlight is absorbed into the device, excitons (electron-hole pairs) are created and diffuse to donor/acceptor interfaces. If the charge carriers are separated at the donor/acceptor interface, the carriers can travel to the respective electrode interfaces for charge extraction.

1.3 The role of interfaces in organic electronics

As seen in Figure 1.1, there are many interfaces within OPV devices. In this thesis I will primarily focus upon the active layer/electrode interface. This interface in particular plays an important role in organic electronics as it is the site of charge injection and extraction from the device. There are many ways to attempt to control the complicated chemistry[13] at the polymer-metal interfaces in an effort to improve device performance. For example, self-assembled monolayers (SAMs) can be used for tuning ITO work functions by placing dipoles at the

interface.[14-16] Note that the original usage of the term "SAM" in the literature commonly refers to the *assembly* of these molecules onto a surface, such as occurs with thiols on gold.[17,18] Though the proposed binding mechanism for phosphonic acid molecules on a transparent oxide[19] likely involves significantly less assembly, organization, and/or re-arrangement in comparison with the thiols on gold, we refer to the phosphonic acid molecule monolayers as SAMs throughout this thesis.

Proper energetic alignment between electrodes and active layer materials is considered paramount to achieving Ohmic contacts and optimal charge extraction from the device.[20,21] SAMs can be deposited using a variety of methodologies,[15,22] one of which is via a patterning technique called microcontact printing. In this thesis, we microcontact print phosphonic acid SAMs as a way to spatially control charge injection in organic electronic devices. A detailed explanation of the stamping (microcontact printing) procedure I use for spatial tuning of the ITO work function can be found in chapter 2, with a discussion of characterization and device implementation following in chapter 3.

Charge carrier recombination is an increasingly important topic in OPV research as it is one of the dominant loss mechanisms.[23-26] Many techniques exist to measure charge carrier recombination, including impedance spectroscopy (IS),[27-29] charge-extraction by linearly increasing voltage (CELIV),[30] transient photovoltage (TPV),[31,32] transient photocurrent (TPC),[32-34] and charge extraction (CE).[32,35,36] O'Regan and Durrant were among the pioneers of the TPV/TPC/CE techniques to investigate charge-carrier lifetimes in dye-sensitized solar cells,[31,37] and their work has since been extended to organic photovoltaics (OPVs).[36,38] Recombination occurs primarily at interfaces within the device, and has been highly studied at the

donor/acceptor interfaces.[23,39-45] However, other interfaces exist in the device, and the properties of the electrode/active-layer interface have also been shown to alter device parameters such as open-circuit voltage (V_{OC}) in OPVs.[16,46-53] As the use of low bandgap donor polymers as a means of increasing V_{OC} and NIR absorption becomes more prevalent, a need for improved interfacial electronic alignment between the electrode and active layer arises. As such, it is conceivable that imperfections in the energetic alignment could lead to band-bending, changes in performance, as well as charge carrier recombination at the electrode/active layer interface. In the literature, the role of the electrode/active layer interface on charge carrier recombination kinetics seems to have received considerably less attention than the roles of the energetics of the donor/acceptor interface.[24] A few studies have measured changes in recombination as a result of electrode/active layer interface modification,[39,47,52,54] and also observe improvements in device performance. Goh and co-workers used SAMs on TiO_2 as interfacial modifiers and measured recombination using transient photovoltage,[47] but to the best of our knowledge there have been no reports of measured recombination differences as a result of using SAMs on ITO in bulk heterojunction OPVs. Thus, herein we describe the use of phosphonic acid SAMs to modify the electrode/active layer interface and correlate changes in device performance with measured differences in carrier recombination. Discussion of the effects of ITO/active layer interface modification with respect to recombination is found in chapter 4.

2 Experimental details

2.1 Introduction

Many techniques are used to control the interfaces in organic electronics as well as study their properties.[14,48,50,55-57] This chapter provides details regarding preparation of patterned self-assembled monolayers on transparent conductive oxides, and also discusses experimental techniques used in this thesis, particularly transient photovoltage and charge extraction.

2.2 Stamping self-assembled monolayers

A poly-dimethyl siloxane (PDMS) stamp with a 5 μm dot pattern was fabricated from a photolithographically patterned silicon wafer master as described elsewhere.[58] In this thesis, the patterned PDMS stamp is used to physically transfer phosphonic acid self-assembled monolayers (PA SAMs) to a transparent conductive oxide (TCO). The stamp pattern feature sizes can vary from ~100 nm to 100s of μm, but are typically on the order of 5 μm. The resulting pattern of SAMs on the TCO can often be verified using various varieties of atomic force microscopy (AFM), including Kelvin probe.[14]

1.5 cm × 1.5 cm ITO coated glass slides (TFD Inc.) were sonicated successively in acetone and then isopropyl alcohol for 20 minutes each. Other TCOs such as indium zinc oxide have been used and can be explored, but the focus of the work herein will be primarily on ITO.

After rinsing the PDMS stamp with ethanol (EtOH) and blowing dry in a stream of nitrogen, a solution of PA in EtOH (10 mM) was swabbed onto the PDMS stamp and blown dry. The solvent cleaned ITO was then air or oxygen plasma cleaned (Harrick Plasma Cleaner PDC-32G, 18W applied), typically for 6 minutes, after which the stamp was immediately pressed onto the ITO surface and held down by a ~35-40 g weight, conveniently provided by DI water in a 20 mL scintillation vial as shown in Figure 2.1 below.

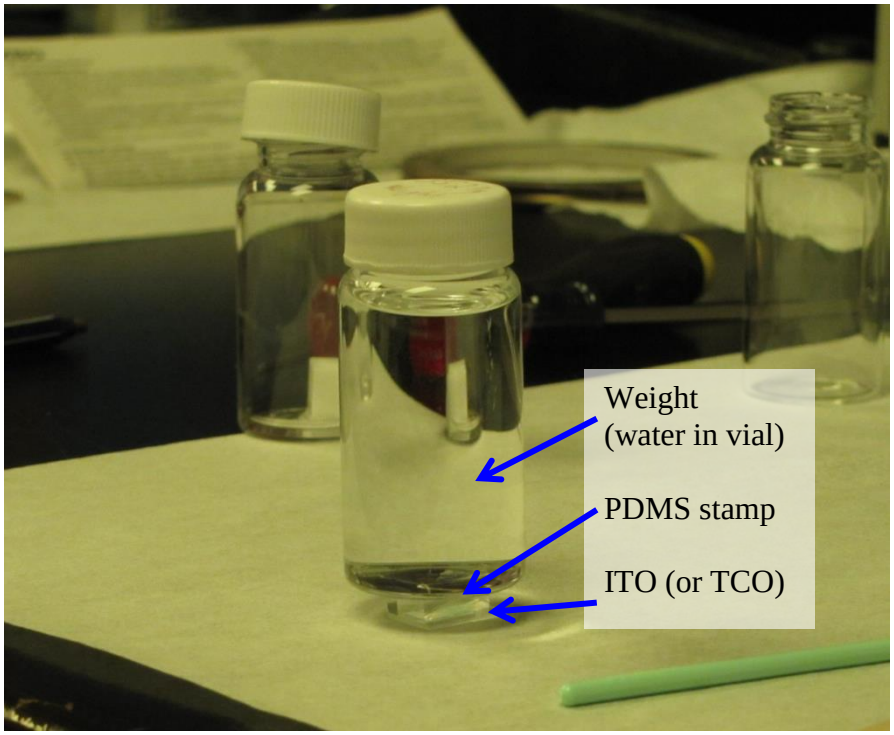

Figure 2.1 Picture of weight used for patterned stamping of PA SAMs on ITO.

After 10 minutes the PDMS stamp and weight were removed and the sample was immediately annealed for 5 minutes on a hot plate which had been pre-heated 140 °C. Following annealing, the sample was removed from the hot plate, rinsed with EtOH, and blown dry in a stream of nitrogen, twice. In reports of preparation of LEDs made with Super Yellow polymer[14] a subsequent basewash step was used in an effort to remove excess non-binding PAs, especially

in “non-patterned” regions of bare ITO. The basewash was comprised of 5% triethylamine:95% EtOH solution (by volume). Hence, samples described in chapter 3 of this thesis were sonicated in basewash for 30 minutes, then rinsed in EtOH, blown dry, and kept covered until loaded into the glove box for active layer deposition. The basewash step was omitted when samples were simply soaked in a 10 mM ethanolic solution of phosphonic acid in Chapter 4.

Following patterning of the SAM, it is possible to “backfill” bare ITO regions with other PA SAMs to e.g. create regions of greater work function contrast. Practically this can be achieved by simply soaking the patterned sample in a solution of a different PA SAM, following the annealing and rinsing steps of the patterning. The backfilling process was not a significant portion of this thesis and has not been optimized, although additional information on patterning and backfilling was reported by Park and co-authors for thiols on gold.[59] Chapter 3 provides additional detail about the use of patterned SAMs in polymer LEDs as a means of spatially controlling injection at the transparent conductive oxide/organic interface.

2.3 Transient photovoltage and charge extraction

2.3.1 Setup and rationale

Transient photovoltage (TPV) and charge extraction (CE) experiments are used to obtain information about charge carrier lifetime and density from working organic photovoltaics. The techniques are also closely related to transient photocurrent (TPC), and cartoon comparisons of the set-ups are shown in Figure 2.2. TPC measurements are acquired under short-circuit conditions, while TPV measurements are made at open-circuit voltage (V_{OC}). Conceptually,

TPV uses a small photovoltage perturbation (often achieved by use of a nitrogen dye laser[32,60,61] or in our case a blue LED), to create a small excess of charge carriers that recombine. The device is held at V_{OC} conditions by connecting the device to a high (1 MΩ) impedance oscilloscope, and is biased with a continuous waveform (CW) white LED. The charge carrier recombination lifetime associated with the photovoltage perturbation is extracted from a single exponential fit of the photovoltage decay. The white light intensity is typically varied over orders of magnitude to control the charge carrier density within the device. Given that the device is tested under V_{OC} conditions, the measured recombination lifetime is considered to primarily represent bimolecular recombination.[60,61] CE is used to measure charge carrier density in the device under a given white light intensity. The device acts like a capacitor and "charges" while the white light is on. When the light turns off, the built-up charge in the device is extracted and used to calculate the amount of charge carriers present in the device.

The TPV and CE setups were modeled after the descriptions in the literature.[32,35,60,62]

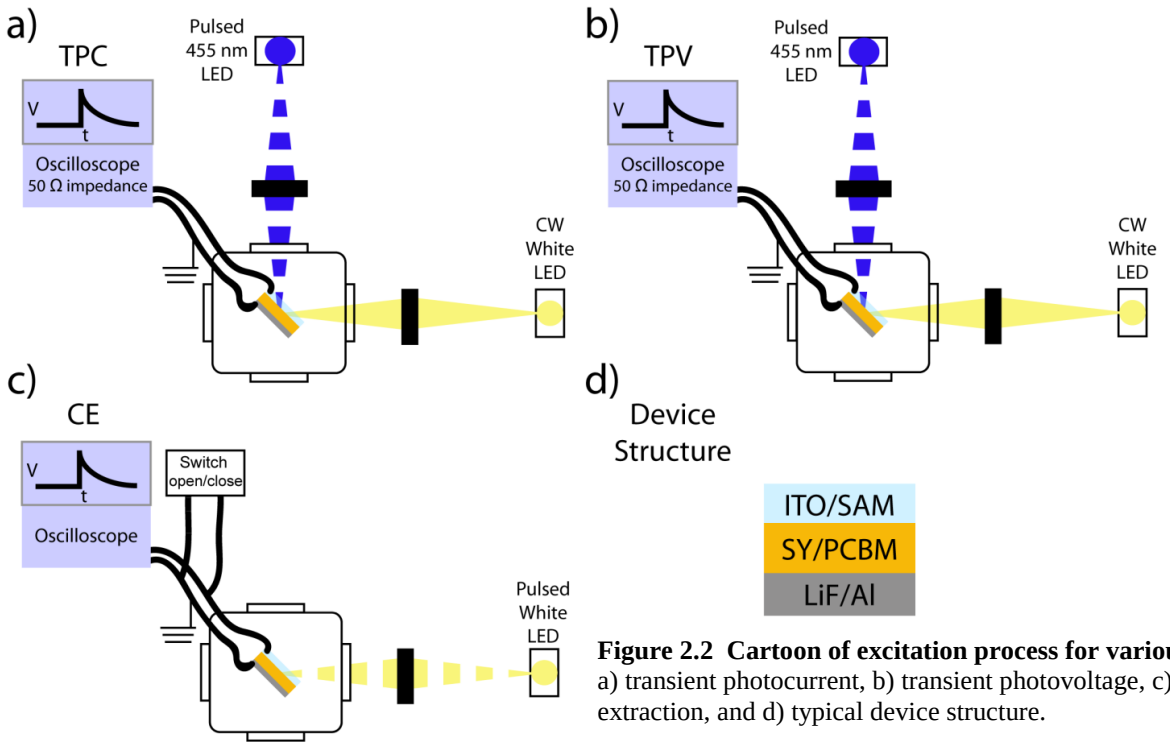

Figure 2.2 Cartoon of excitation process for various techniques. a) transient photocurrent, b) transient photovoltage, c) charge extraction, and d) typical device structure.

However, some key differences include the use of a pulsed 455 nm LED instead of a laser for the transient photovoltage experiments, and the use of a homebuilt charge extraction circuit herein referred to as "the black box". Details of the circuitry inside the black box can be found on KMK_VI149, noting that the charge extraction switch is now located externally to the black box. Figure 2.3 shows some schematics of the instrument equipment connections for transient photovoltage, transient photocurrent, and charge extraction experiments.

Before delving into the data processing and calculations, it is beneficial to discuss the nature of the chosen data measurement conditions noted in Figure 2.3. Beginning with TPV, the

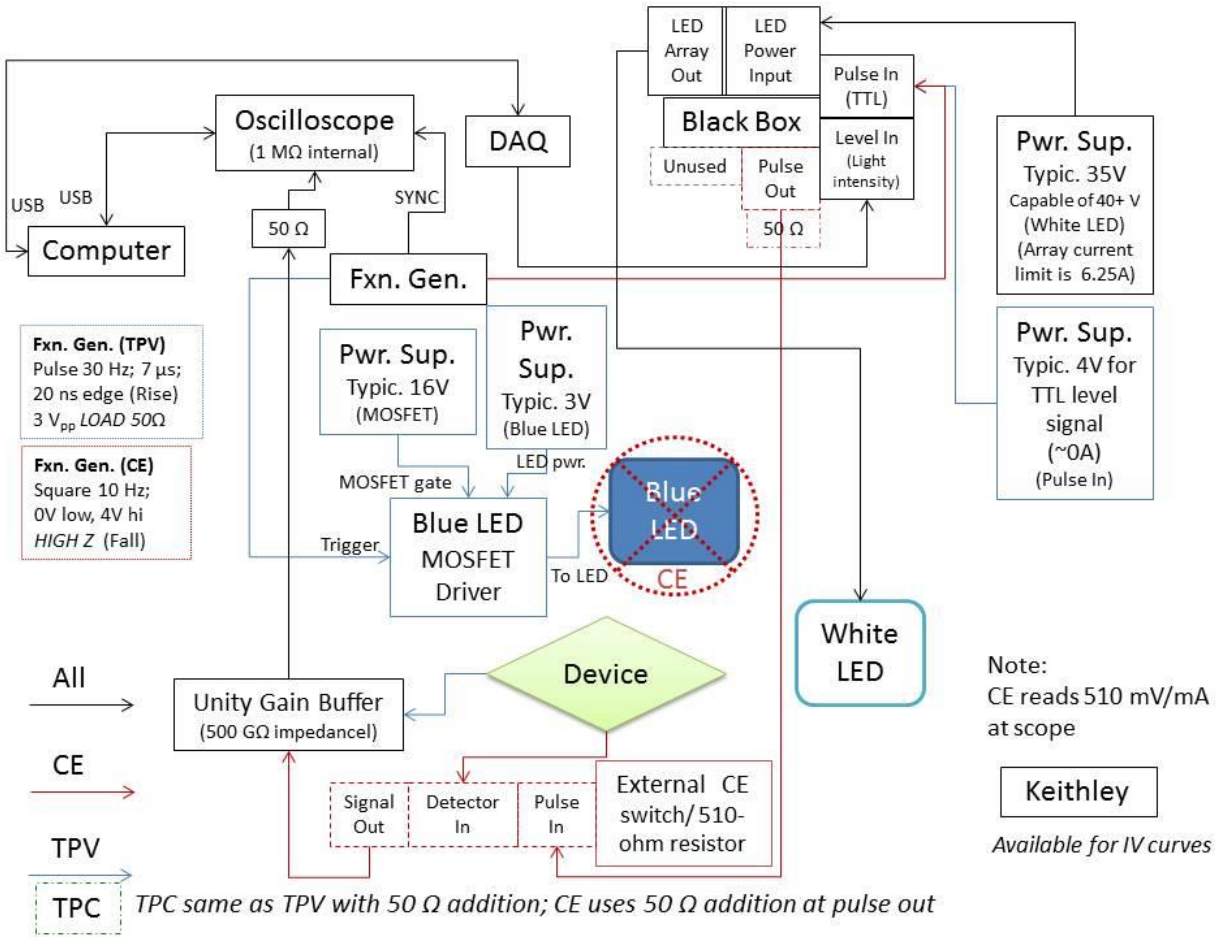

Figure 2.3 Schematic of instruments and connections used in transient photovoltage (TPV), transient photocurrent (TPC), and charge extraction (CE) measurements.

blue LED that provides the perturbation has a homebuilt MOSFET driver circuit that is used in conjunction with a function generator to pulse the LED at a typical rate of 30 Hz, with a 4 μs pulse width, and a 20 ns rising edge. The pulse width is as narrow as possible while still allowing for complete LED turn-on. Note that the pulse width imposes a limit on the shortest measurable TPV recombination lifetimes, and that measured recombination lifetimes can be extremely sample dependent. If faster lifetime measurements are desired, use of a pulsed laser (e.g. nitrogen dye laser)[32] should be considered.[63] Next, the repetition rate is also determined by how quickly the LED can turn on and off, as adequate time is needed to allow the LED to equilibrate to the on or off position. The driver circuit takes the trigger information (output from the function generator) and the current/voltage to drive the LED (from blue LED power supply), and uses a fast MOSFET (requiring 15-18 V to be dropped across it) to send the voltage/current pulses to the LED.

If the TPV results are to be compared to CE results, the same white LED light source and position must be used for both experiments. The white LED is used in CW mode, i.e. constant illumination during the TPV measurements. During the CE experiment, the white LED is switched on and off through the black box that also syncs with the opening and closing of the external charge extraction switch. In essence, the sample device acts as a capacitor and accumulates photocarriers while the light is on (typically square wave, 10 Hz, 50% duty cycle) and the switch is open, and then as the LED is turned off the switch closes, allowing the equilibrated charge in the device to be measured at the oscilloscope. The intensity of the white LED in both TPV and CE experiments is determined by the "Level In" input on the black box and the USB-connected data acquisition card (DAQ) that is user-defined via LabView. If the

DAQ outputs 1V, the corresponding current to the LED will be 1A. Note that the current to the white LED will be displayed on the white LED power supply. It is highly recommended to limit the current through the power supply below the maximum current rating of the LED in order to minimize the likelihood of destroying the LED, even when the LED is pulsed. During CE measurements, the function generator is input into the "pulse in" on the black box, and provides both the time characteristics of the white light output, as well as the 4V output to the TTL circuit (refer to KMK_VI149). When the white LED is operated in CW mode as for TPV measurements, a power supply or equivalent can supply the needed 4V.

The device output always passes through a unity gain buffer (UGB) prior to measurement at the oscilloscope. Without this circuit, there are inconsistencies in the device V_{OC}

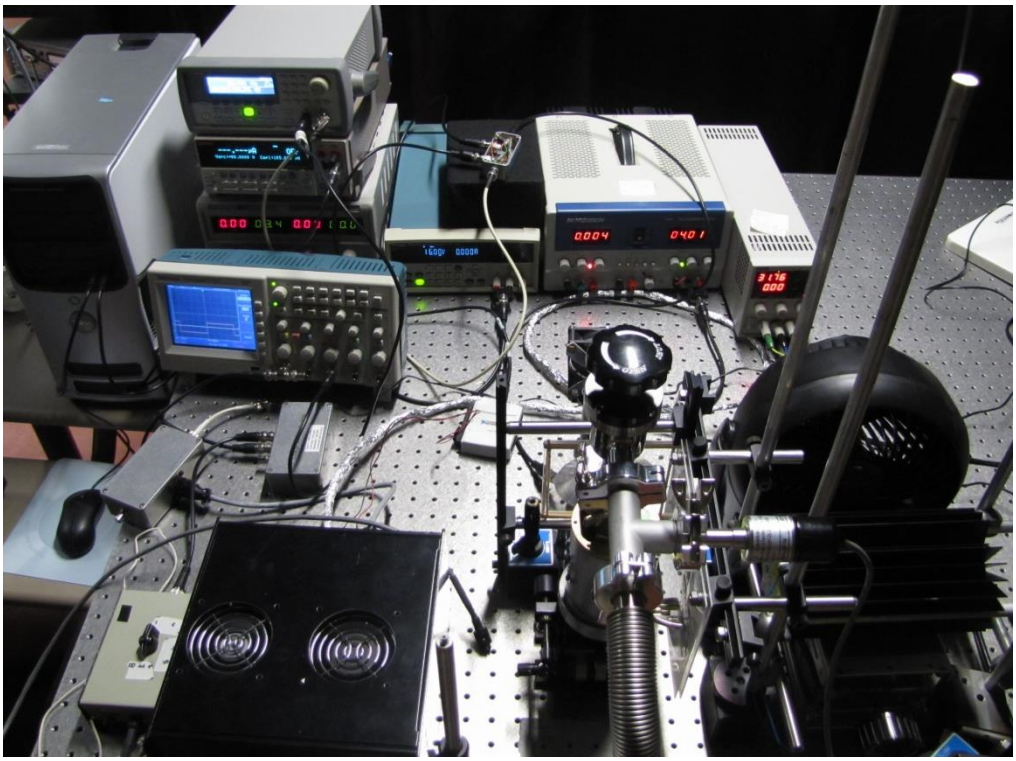

Figure 2.4 Photograph of the TPV/CE device testing bench.

measurement between the Keithley and the oscilloscope, originating from a combination of the difference in impedance between the Keithley and the oscilloscope (10 GΩ versus 1 M Ω, respectively), as well as the low current output from our small cell areas (typically <0.0386 cm^2). Measurement errors without the UGB are particularly noticeable at lower light intensities. The UGB has an impedance of 500 GΩ, and requires a termination of 50 Ω at the oscilloscope to mitigate the ringing created. A photograph of the TPV/CE testing bench, including the relevant instrumentation and UGB, is shown in Figure 2.4.

2.3.2 Data processing

Below is an overview bullet list of the steps used in charge extraction data processing, drawn from literature examples.[32,35,60] I have written multiple versions of the data processing Igor Pro procedure file as the setup advanced, but the general steps are outlined below. See Appendix A for a detailed list of various code versions.

<u>To calculate charge carrier lifetime ($\tau_{\Delta n}$):</u>

- Acquire voltage transient (raw from oscilloscope) → normalize initial peak amplitude to 1 (not strictly necessary but simplifies group fitting routine).
- Use Igor Pro to fit an exponential over several decay lifetimes (exp_x offset can be used to calculate single exponential fits and dbl_exp_xoffset can be used to calculate an exponential fit for the sum of 2 exponential decays; ideally extend the fit over 2-3 lifetimes).

- Relevant equation: $\Delta V = \Delta V_0 e^{-\frac{t}{\tau_{\Delta n}}}$ as described by Maurano and co-workers,[32] where the change in voltage, ΔV, created by the blue LED pulse is described by a decaying single exponential over time, *t*, with a decay lifetime, $\tau_{\Delta n}$. ΔV_0 is the transient amplitude. The exponential fit lifetime, τ, is represented by $\tau_{\Delta n}$ in the equation above as a way of indicating that the lifetime, is affected by changes in carrier density, Δn.

- Plot $\tau_{\Delta n}$ vs V_{OC}.

<u>To calculate charge carrier density (*n*) by volume (cm^{-3}):</u>

- Voltage transient (raw from oscilloscope) → current transient (using V=IR; presently R=511 Ω in charge extraction switch)
- Current transient → current density (divide current by masked pixel area (0.0136 cm^2))
- Subtract background noise if applicable, and any voltage offsets (ensure appropriate units, this step can essentially be done at any point during the calculation of current per volume).
- Current density (A/cm^2) / device thickness (cm) → Current per volume (A/cm^3)
- (optional plot of curves to be integrated) y = $Amps/cm^3$ vs x = time (sec)
    - My procedure also generates a plot that shifts the x-axis of the current volume data so that the light "off" occurs at time = 0 sec. A subsequent plot also truncates the current volume wave prior to t=0 since the entire "truncated" wave is integrated during the subsequent integration step.

- Use Igor Pro (or other software) to integrate over the complete decay time scale (definite integral); the area under the curve corresponds to the extracted charge carrier density.
- Numerical answer is in units of C/cm^3, so divide by charge on an electron ($1.602e^{-19}$ C) to calculate charge carrier density in units of 1/cm^3.

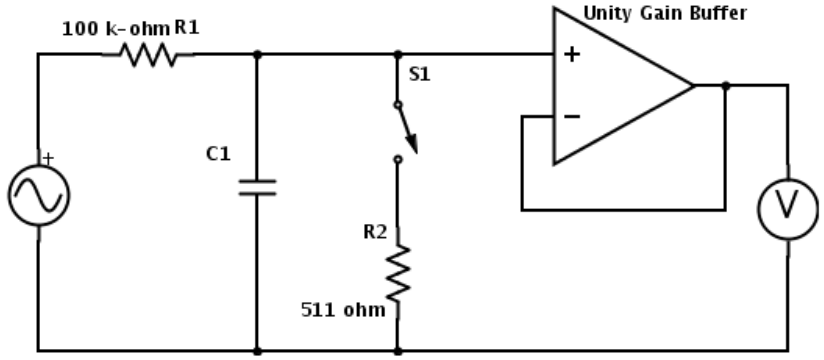

Figure 2.5 Circuit diagram for capacitor calibration of charge extraction circuit. The inclusion of the 100-kΩ resistor, R1, is to direct charge away from the function generator and over the path of lower resistance, the 511 Ω resistor (R2) in the charge extraction circuit.

2.3.3 Calibration of charge extraction measurement

During the charge extraction experiment, the device builds up charge under a light bias and then releases the charge via a switch when the light is turned off. The device functional operation is analogous to a capacitor, and we calibrate the charge extraction circuit using commercial capacitors of 1 nF, 5.6 nF, and 22 nF. Instead of charging the capacitors with a light bias as typically occurs for a photovoltaic device, the function generator provides a 4V square wave that is synced in time to the charge extraction switch (refer to Figure 2.3). A capacitor is >99% charged after five time constants (T=RC). Charging occurs when the switch is open, and so the time constant is determined by the resistor, R1. The slowest charging time (largest

capacitor), is calculated as 2.2 ms. Thus, the function generator is set to 10 Hz (i.e. a period of 100 ms) which allows ample time for any of the capacitors to be fully charged before discharging over R2. The calibration circuit schematic is shown in Figure 2.5.

The voltage decay measured at the scope is converted to current using Ohm's Law (V=IR), where R=resistance in the charge extraction switch, 511 Ω. The plot of current vs time is then integrated to calculate charge, q. Given a known capacitance, C, and a known applied voltage, V, we expect the circuit should measure: (CV=q)

C = 1 nF; V = 4V; therefore q = 4 nC

Some of the measured data are shown in Figure 2.6, and all are summarized in Table 2.1.

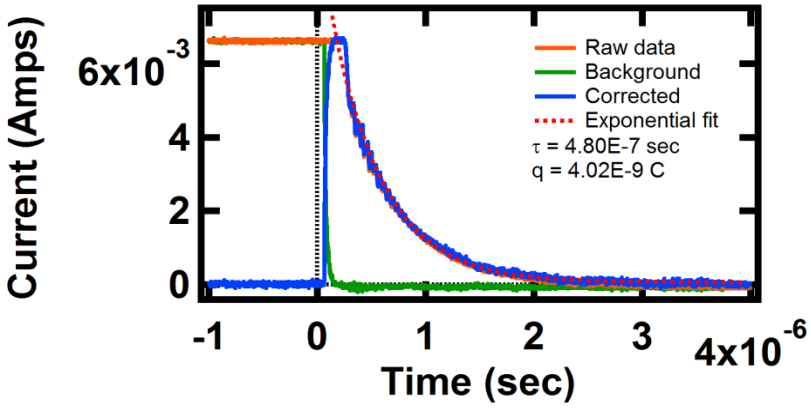

Figure 2.6 Decay of calculated current from 1 nF capacitor, as measured by charge extraction circuit. Raw data is shown in orange, the background (no capacitor in circuit) is shown in green. The corrected data (blue) is acquired by subtracting the background (green) data from the raw (orange) data. A single exponential fit to the corrected data is a good fit (red dashed curve).

The corrected data shown in Figure 2.6 is integrated and used to calculate q to be 4.02 nC, which is in good agreement with the expected 4 nC. Additionally, we validate the accuracy of our measurement system by fitting a single exponential ($y = y_0 e^{-\frac{t}{\tau}}$) to the current decay, and comparing the lifetime, τ, to the expected time constant of the capacitor (τ=RC). For a 1 nF

capacitor, C, and a resistor of 511 Ω, R, we expect a time constant, τ, of 0.51 μs. The single exponential fit is shown as a red dashed line in Figure 2.6 Decay of calculated current from 1 nF capacitor, as measured by charge extraction circuit.Figure 2.6, and yields a lifetime of 0.48 μs. The relevant data for all three tested capacitors is shown below in Table 2.1.

Capacitance (nF)	Expected q (C)	Measured q (C)	Expected τ (s)	Measured τ (s)
1	4.00×10^{-9}	4.02×10^{-9}	5.10×10^{-7}	4.80×10^{-7}
5.6	2.24×10^{-8}	2.15×10^{-8}	2.86×10^{-6}	2.77×10^{-6}
22	8.80×10^{-8}	8.95×10^{-8}	1.12×10^{-5}	1.15×10^{-5}

Table 2.1 Expected and measured values of charge, q, and lifetime, τ, for commercial capacitors using the CE circuit.

2.3.4 Testing inverted architecture photovoltaic devices

Though the emphasis of this thesis is almost exclusively focused on standard architecture photovoltaic devices, the TPV and CE setup can easily accommodate inverted architecture devices. The charge extraction switchbox has a polarity toggle (pos/neg) located on the exterior of the switchbox. The fast switches used in the switchbox have limited voltage ranges, and so different switches are used for either positive or negative photovoltages. The resistance the charge is dropped across, 511 Ω, does not change.

For standard architecture devices, the toggle should be set to “pos”, and for inverted devices, “neg”. Note that the inverted device photovoltage will appear as negative on the oscilloscope. The data can be inverted on the scope, then collected and processed through the

Igor code as usual, or inverted during data processing using Load_OE_Files4 Igor procedures or earlier. Additional Igor Pro data processing details are provided in Appendix A.

3 Spatially modulated interfacial properties

3.1 Introduction[a]

The polymer-electrode interface can critically affect the performance of organic electronic devices, including thin-film transistors (TFTs), organic light emitting diodes (OLEDs), and organic photovoltaics (OPVs). Self-assembled monolayers (SAMs) have been used to modify the surface chemistry of polymer,[64,65] metal,[66-72] and metal oxide[73-79] electrodes in order to control properties including wettability, work function, and charge transfer, by using many functional group/substrate combinations. Examples range from thiols on gold,[66-71] to silanes on hydroxyl-terminated surfaces,[74,75,78,80] to mixtures of SAMs containing different terminal functional groups on metal oxide buffer layers.[76] A number of groups have incorporated SAMs into OLEDs,[64-68,73-75,81,82] particularly the use of phosphonic acid SAMs to modulate interfacial properties and improve device performance.[83-89]

Given the strong influence SAMs modifiers can have on the performance of organic electronic devices, the ability to microcontact print SAMs with large work function contrast is both scientifically interesting from the standpoint of creating model systems to explore the role of barriers and energy level offsets on charge injection in OLEDs, and technologically useful in the context of applications including low-cost fixed displays.[66,68] Moreover, because of the ease in visualizing the changes in electrode work function through patterned OLED

[a] This chapter is adapted from: K. M. Knesting, P. J. Hotchkiss, B. A. MacLeod, S. R. Marder, and D. S. Ginger. *Advanced Materials*. **2012**, *24*, 642–646.

electroluminescence, it is possible to more easily inspect the effect SAMs have on injection and extraction into the organic material, which can also be applied to OPVs.

Although a limited amount of work has investigated the use of electrodes with patterned work function, notably by microcontact printing thiols on gold,[66,68] silanes on hydroxyl-terminated surfaces,[65,74,75] or phosphoryl chlorides on indium tin oxide (ITO),[90] these functional group/substrate combinations are not necessarily ideal for integration into OPV and OLED applications. First, transparent conductive oxides are more commonly used than gold as the anode in OPVs and OLEDs. Second, silanes can be microcontact printed onto oxides, but can often exhibit spreading and poor fidelity unless they are microcontact printed onto hot substrates.[81,82] Fujihira and co-workers shifted the ITO work function using benzoyl- and phosphoryl- chlorides,[91,92] and microcontact printed these molecules to give patterned electroluminescence.[90] However, the resulting contact potential difference (CPD) between patterned and unpatterned SAM regions of the ITO substrate was significantly lower than the CPD shift measured on ITO that had been soaked in a SAM solution, perhaps suggesting poorer ordering or lower density of the microcontact printed SAMs relative to solution-deposited SAMs. Blom and co-workers also observed lower-than-expected CPD contrast from an analogous microcontact printed thiol-SAM on gold system, reporting that their microcontact printed SAMs imparted a change in work function that was only 10% of the shift in work function achieved by solution deposition of the SAM.[66]

Here, we overcome these difficulties using patterns of pentafluorobenzyl phosphonic acid (F_5BnPA) deposited *via* microcontact printing to locally modify the ITO work function. We measure CPD variations of ~ 500 mV between the modified and unmodified areas of the ITO

surface from microcontact printed F_5BnPA. The high contrast resulting from our microcontact printed patterns is observable both in scanning Kelvin probe microscopy (SKPM) images and in corresponding electroluminescence images of LEDs fabricated on the same sample from which the SKPM images were collected. Comparisons of LED device performance between microcontact-printed SAM LEDs and solution-soaked SAM LEDs suggest that we achieve comparable SAM densities on both the microcontact-printed areas and solution-soaked SAM devices, indicating large, consistent changes in charge injection across the microcontact-printed surfaces.

3.2 Results and discussion

Fig. 3.1 shows a schematic of our approach, along with structures of the materials used and the relative energy levels expected for modified and unmodified ITO surfaces. Det. Cl. is detergent solvent cleaned ITO,[93] AP is air plasma cleaned ITO,[86] and SY is Super Yellow.[57,94]

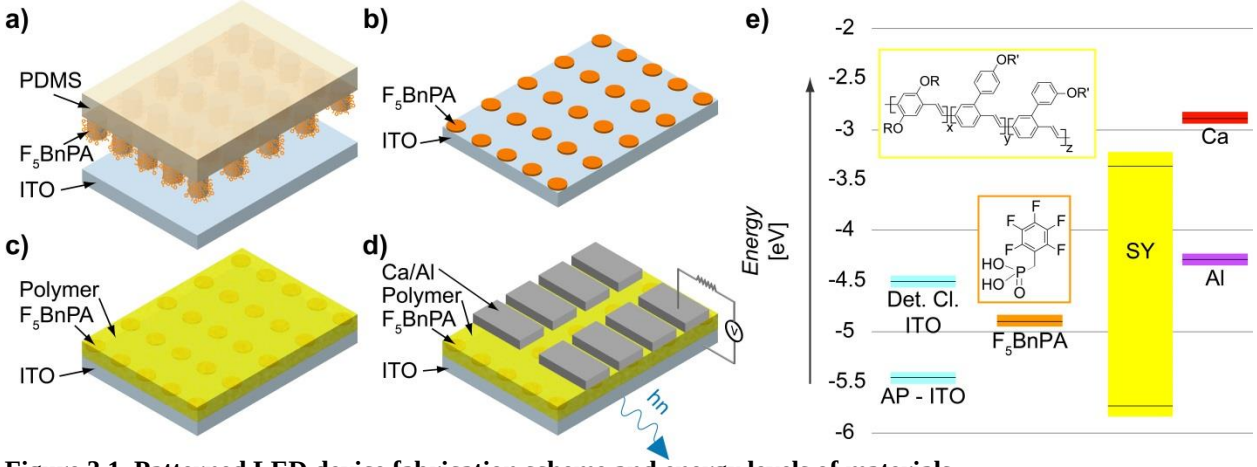

Figure 3.1 Patterned LED device fabrication scheme and energy levels of materials.
a) F_5BnPA inked PDMS stamp is brought into contact with freshly plasma cleaned ITO. b) Upon removal of the stamp, the patterned SAM remains on the substrate. c) Polymer is spin-coated on top of SAM. d) Ca and Al electrodes are evaporated on top of the polymer to complete device fabrication. e) Comparison of energy levels for relevant device materials and selected structures are shown.

The work functions of F_5BnPA,[86,93] Ca, and Al are also shown.[95] We chose F_5BnPA as the modifier, in part because previous work has shown that F_5BnPA can improve the performance of small molecule OLEDs,[86] and because an ITO surface modified with F_5BnPA is compatible with spin-coating of many conjugated polymers.

We deposited F_5BnPA patterned layers using standard microcontact printing methods. Briefly, a poly-dimethyl siloxane (PDMS) stamp with a 5 μm dot pattern was fabricated from a photolithographically patterned silicon wafer master as described elsewhere.[58] The PDMS stamp was inked and pressed into contact with the ITO for 10 minutes, and then the sample was immediately annealed on a pre-heated 140°C hot plate for 5 minutes. This brief anneal is believed to help promote binding of the phosphonic acid.[96,97]

We used Atomic Force Microscopy (AFM) and SKPM to characterize the resulting patterns. Fig. 3.2 shows both the topography and the potential image, along with line traces, for the same area of the sample. Unsurprisingly, the topography image in Fig. 3.2A shows little

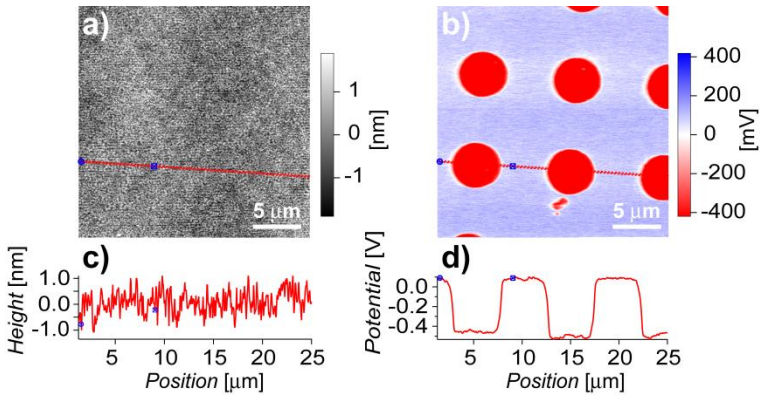

Figure 3.2 SKPM images and line traces of microcontact printed F_5BnPA on ITO.
a) Height image and corresponding line trace. The blue tick marks on the line trace correspond to image positions as a guide to the eye. b) Potential image and corresponding line trace. The red regions show the location of the microcontact printed SAM, at a potential difference of about ~0.55 V below the surrounding ITO (light blue regions). The contact potential difference (CPD) of ~0.55 V is within 0.1 V of the literature values for ITO samples soaked in the SAM solutions. The lack of large topography (a) and uniformity of the CPD (b) are consistent with single layer coverage.

contrast since the height of a vertical F_5BnPA monolayer (~0.9 nm) is comparable to the root mean squared (RMS) roughness (~ 0.7 to 0.8 nm) of the ITO. We interpret the lack of significant topography in Figs. 3.2A and 3.2C as evidence that the microcontact printing procedure does not leave behind F_5BnPA aggregates or multilayers on the ITO surface. On the other hand, the potential image in Fig. 3.2B clearly shows evidence for deposition of the F_5BnPA by the microcontact printing procedure. The 5 μm-diameter red circles in the potential image in Fig. 3.2B are indicative of the microcontact printed F_5BnPA regions, while the blue background is bare ITO. Fig. 3.2D shows a line trace of the potential data along the section indicated by the red line in Fig. 3.2B. The trace shows both that the interface between the SAM and unpatterned ITO is fairly sharp (~300 to 500 nm, 10%-90% ΔV) and that the contrast in contact potential difference between the patterned and unpatterned regions is uniformly ~ 0.55 V. These are both significant observations. First, the edge resolution suggests that the F_5BnPA molecules do not diffuse rapidly on the surface during the contact time or the thermal anneal. Previous studies utilizing both polarization modulation infrared reflection adsorption spectroscopy (PM-IRRAS)[93] and density functional theory[98] have suggested that phosphonic acids likely bind to metal oxides through a bidentate attachment. We hypothesize that this fact, along with hydrogen bonding between the SAM molecules, and between the SAM and substrate, could serve to reduce diffusion of the phosphonic acids across the surface, thus improving the pattern contrast and resolution compared to that obtained with previous studies of patterned SAMs on ITO. Second, the 0.55 V CPD contrast is in good agreement with the 0.5 eV shift in ITO work function reported upon surface modification with F_5BnPA via literature methods.[86,93] Furthermore, the

0.55 V CPD is ~10× larger than the CPD previously reported using microcontact printed 4-chlorophenylphosphoryl dichloride on ITO.[90]

We next evaluate the performance of the F_5BnPA-microcontact printed ITO substrates as anodes in OLED devices incorporating the commercially available polymer Super Yellow (SY) (EMD Chemicals, PDY-132), and Ca/Al as the top contacts. The device structure is depicted in Fig. 3.1. We compare ITO anodes that had been modified with F_5BnPA deposited from solution, ITO anodes with microcontact printed F_5BnPA deposited by microcontact printing, and control devices with bare, unmodified ITO anodes (treated identically to the solution-coated anodes, except for the F_5BnPA exposure). Fig. 3.3 shows the luminance-voltage and current-voltage characteristics of electroluminescent devices with the various ITO modifications. As expected, the presence of the F_5BnPA SAM, regardless of deposition technique, significantly increases the device luminance (Fig. 3.3A) and also improves the current density (Fig. 3.3B) compared to the

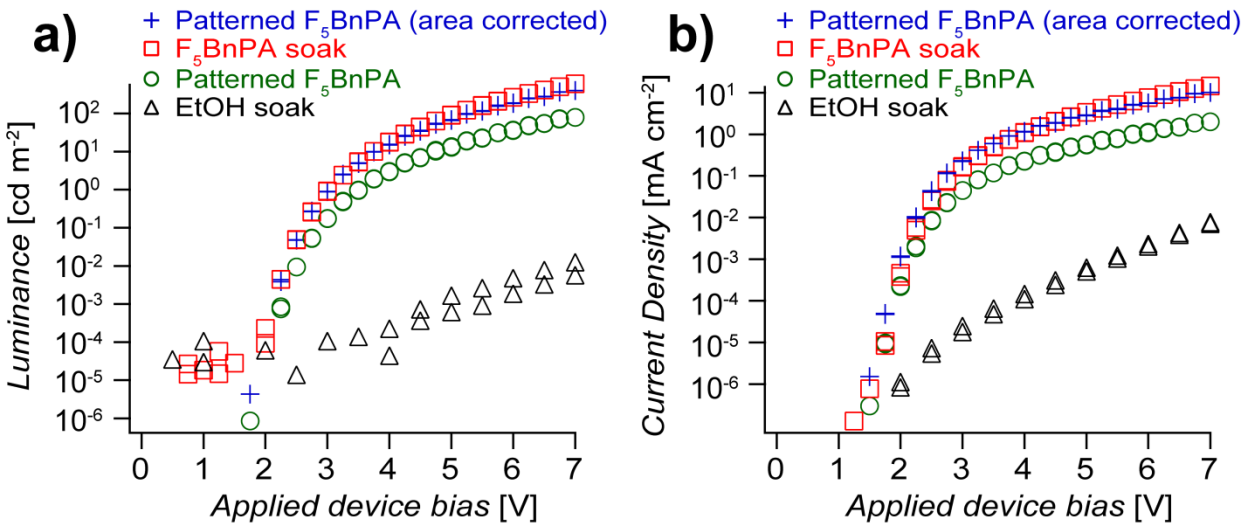

Figure 3.3 Comparison of device characteristics between patterned and SAM-soaked samples. SAM soaked sample (red square), patterned sample (green circle), ethanol soaked control (black triangle), and the pattern adjusted for the electroluminescence area (blue cross) are compared. a) Luminance comparison by sample type as a function of applied device bias. b) Current density as a function of applied device bias for SAM-soaked, patterned, and control devices. As expected, the presence of the F_5BnPA SAM requires less applied voltage for current to flow through the device than control (ethanol soaked) LEDs.

control device incorporating unmodified ITO. For example, at 5 V bias, the current density on the F_5BnPA-modified substrates is ~5 orders-of-magnitude higher than the unmodified ITO, while the luminance is ~3.5 orders-of-magnitude higher than on unmodified ITO. The increased device performance can be attributed to the improved charge injection from the energy level alignment between F_5BnPA and the SY highest-occupied molecular orbital (HOMO), compared to that for unmodified ITO (see Fig. 3.1).[86,93,94,99] The microcontact printed F_5BnPA sample exhibits slightly lower total luminance and current density for a given applied bias when compared to the soaked F_5BnPA SAM device since only ~20% of the surface was modified. When normalized for the area covered with F_5BnPA on the microcontact printed substrate (Fig. 3.3, blue cross traces), the luminance and current density of the microcontact printed devices are nearly identical to the solution soaked substrates (Fig. 3.3, red squares and blue crosses). This excellent agreement between the microcontact printed and bulk-soaked samples is a strong indication that we have achieved similar SAM coverage with both deposition techniques, further supporting the high-fidelity potential data (Fig. 3.2) collected on the same device.

Fig. 3.4 shows optical microscopy images of the patterned electroluminescence. The regions of bright electroluminescence occur at a pitch of 10 μm (center-to-center) that coincides with the dimensions of the microcontact printed F_5BnPA pattern, and the uniform circles of patterned electroluminescence in Fig. 3.4A agree well with the uniform potential contrast observed on the same substrate as that shown in Fig. 3.2. We note that with a well-inked stamp, the microcontact printing technique can provide uniform patterning over a large area, as evident by the uniform electroluminescence pattern in Fig. 3.4B. We attribute the occasional missing dots in the images to defects in the stamp (missing posts, visible upon inspection of the stamp

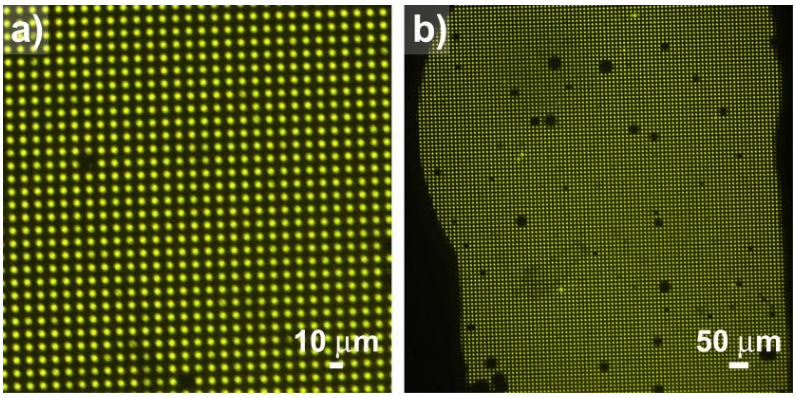

Figure 3.4 Electroluminescence images of patterned F_5BnPA LED. Electroluminescence is from same device as shown in Figure 3.2 SKPM data for small area (a) and large area (b). Electroluminescence was acquired at 5V applied device bias. SAM containing areas emit electroluminescence while the bare ITO regions remain dark. The overall pattern uniformity is in good agreement with the SKPM potential scan.

under an optical microscope) and/or dark spots[100,101] (seen on both patterned and unpatterned samples) that are commonly observed upon microscopic inspection of LEDs.

These results demonstrate that local control of the ITO work function can be obtained using microcontact printing to pattern phosphonic acid SAMs and achieve surface contact potential difference contrast of over 0.5 V, comparable to those obtained from solution-deposited SAMs. The ability to pattern phosphonic acids with low cost printing may find use in applications including low-cost LED signage.[66,68] Given the robust nature of the microcontact printed SAM patterns, it should be possible to use backfilling of a second SAM to tailor the local work function and wettability contrast on both the patterned and unpatterned regions.[59] The microcontact printing of phosphonic acid modified catalysts for in situ polymer growth[72,102] is also an area of significant future interest. Finally, while LEDs were used as an easily visualizable test bed, the successful incorporation of microcontact printed phosphonic acid SAMs into solution-processed polymer diodes opens the door for the use of similar microcontact printed SAMs on a range of transparent conductive oxides[103] in OPV applications, perhaps to

control film morphology,[59,104,105] in addition to local energy level alignment and carrier selectivity at a contact.

3.3 Experimental

1.5 cm × 1.5 cm ITO coated glass slides (TFD Inc.) were sonicated successively in acetone and then isopropyl alcohol for 20 minutes each. Following sonication, clean slides were masked by Scotch tape for etching with HCl/Zn to create an active area strip of 0.9 cm wide ITO. After etching, the slides were scrubbed with detergent (Micro-90) and deionized (DI) water, then rinsed in DI water and again sonicated in acetone and then isopropyl alcohol for 20 minutes each.

After rinsing the PDMS stamp with ethanol (EtOH) and blowing dry in a stream of nitrogen, a solution of F_5BnPA in EtOH (10 mM) was swabbed onto the PDMS stamp and blown dry. The solvent cleaned ITO was then air plasma cleaned (Harrick Plasma Cleaner PDC-32G, 18W applied), typically for 6 minutes, after which the stamp was immediately pressed onto the ITO surface and held down by a ~35-40 g weight. After 10 minutes the stamp was removed and the sample was immediately annealed on a pre-heated 140 °C hot plate for 5 minutes. Following annealing, the sample was removed from the hot plate, rinsed with EtOH, and blown dry in a stream of nitrogen, twice. Samples were then sonicated in a 5% triethylamine:95% EtOH solution (by volume) for 30 minutes, then rinsed in EtOH, blown dry, and kept covered until loaded into the glove box for active layer deposition.

SKPM was performed using an Asylum Research MFP-3D atomic force microscope (AFM) with custom software written in Igor Pro, a Stanford Research Systems SR 830 lock-in amplifier, an Agilent 33120A waveform generator, and a home-built summing amplifier.[106] An AC voltage of 2 V was applied at a frequency of 700 Hz to the tip. A BudgetSensors Tap300E Cr/Pt scanning probe (nominal 300 kHz resonance frequency and 40 N m^{-1} force constant) was used for imaging, and all measurements were made in non-contact mode. During SKPM scans, the tip lift height was 50 nm. The lock-in amplifier was used to detect any phase-shift in the cantilever response at the frequency of the AC-voltage, and a feedback loop in the MFP-3D controller was used to apply a DC voltage to the tip to null out this AC phase shift.

After deposition of the SAM on ITO, a warm (45-50 °C) 5 mg/mL toluene solution of SY (used as received) was spin-coated on the sample in a dry nitrogen glove box (<5 ppm O_2 and <0.1 ppm H_2O, typical), yielding a film thickness of 97 nm (measured with a KLA Tencor Alpha Step 500 Surface Profiler). To complete the devices, 10 nm of calcium metal (Ca, 99.99%, Aldrich) was thermally evaporated at a pressure of 4×10^{-7} Torr, rate = 0.8 Å s^{-1}, followed by 55 nm Al (0.062" diameter Al wire, 99.999%, Lesker) at a pressure of 2×10^{-7} Torr, rate = 1.5 Å s^{-1}, in a glove box integrated evaporator (Angstrom Engineering Amod 600 series). Vacuum was broken (to glove box atmosphere) in between evaporations in an effort to minimize shadowing effects through identical fixed source placement.

Device current-voltage and luminescence characteristics were acquired using custom LabVIEW software, a Si photodiode, and Keithley 2400 in a dry nitrogen glove box (<1 ppm O_2 and <0.1 ppm H_2O, typical). Electroluminescence images were acquired from devices in a homebuilt vacuum chamber, through an inverted microscope (Nikon TE2000-U, LU Plan Fluor

10X objective, WD 15, NA 0.30) with an intermediate 1.5X lens (total magnification of 15X), and integrated CCD camera (Diagnostic Instruments Spot Flex). Electroluminescence spectra were collected through the microscope using an Ocean Optics CCD (1000 ms integration, 150 averages) and were not corrected for the transmission of the optical system.

4 Recombination on SAMs-modified interfaces

4.1 Introduction[b]

Organic photovoltaics (OPVs) are widely studied as a potential low cost alternative to traditional photovoltaic technologies. Over the last few years, reported efficiencies have increased rapidly, and now approach 9.2% in single junction cells,[107] and over 10% in multijunction cells.[1,2] Further improvements to approach proposed theoretical limits[108-110] for OPVs will require identifying and mitigating carrier recombination losses that reduce the open-circuit voltage (V_{OC}) and fill factor in OPVs. To this end, a considerable amount of effort and progress has already been made,[23-26] especially in studying recombination at the donor/acceptor interfaces of bulk-heterojunction (BHJ) solar cells.[23,43,44,60]

Nevertheless, other interfaces exist in the device, and the properties of the electrode/active-layer interface are known to alter device parameters such as V_{OC} in OPVs.[16,46-53] While a handful of studies have measured changes in recombination as a result of electrode/active layer interface modification,[39,47,52,54] our understanding of the role interface modifiers play remains incomplete.[16] Furthermore, synthetic chemists continue to develop polymers with increasingly more positive oxidation potentials and NIR absorption to increase V_{OC},[111,112] making it likely that interfacial effects at the hole extracting contact will play an

[b] This chapter is adapted from: K. M. Knesting, C. W. Schlenker, A. J. Giordano, H. Ju, O. L. Smith, A. Garcia, D. C. Olson, S. R. Marder, D. S. Ginger. *In preparation.*

increasingly more important role in determining charge collection efficiencies in next-generation devices.

In chapter 4, we study the effects of phosphonic acid self-assembled monolayers (PA

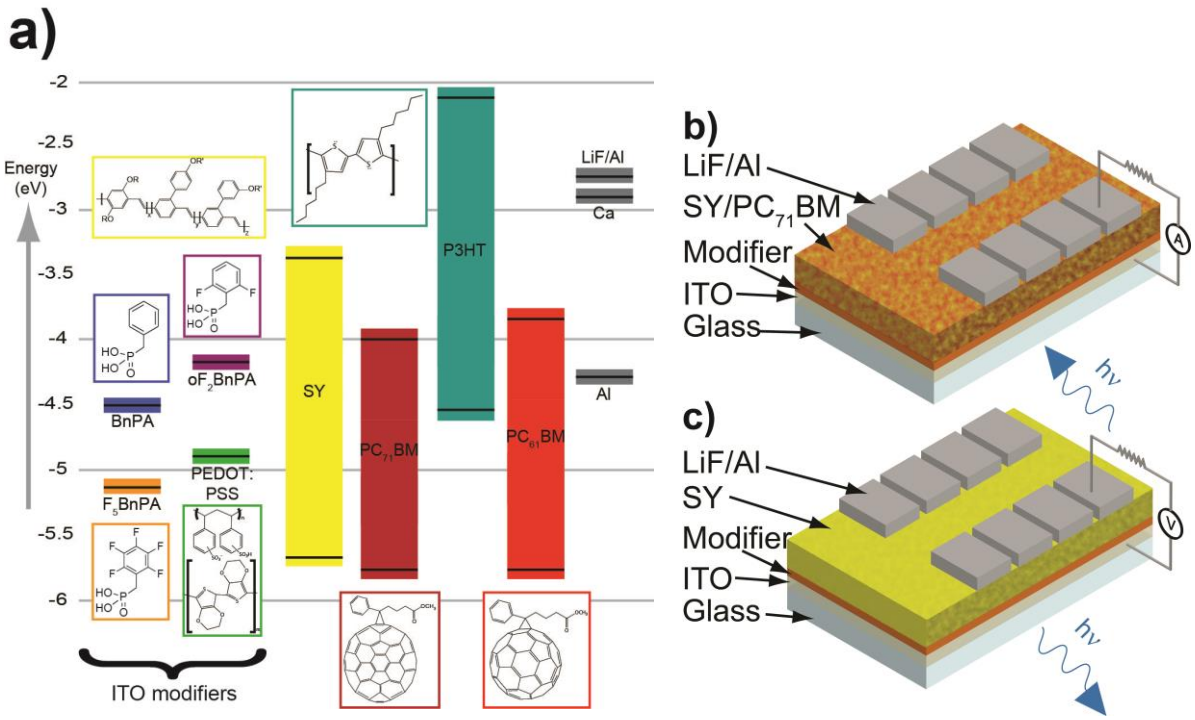

Figure 4.1 Relevant energy levels, structures, and device architectures.
(a) Relevant energy levels and structures of materials used in device fabrication. (b,c) Device architectures for SY/$PC_{71}BM$ OPVs (b), and SY-only LEDs (c). P3HT/$PC_{61}BM$ devices were fabricated similarly to b, as described in the experimental.

SAMs) on the V_{OC} and recombination kinetics in model OPV devices. PA SAMs provide a versatile, simple method of altering the electrode/active layer interface in OPVs by modifying the ITO work function,[14,19,57,93] and thus tuning V_{OC}.[15,16] We use Super Yellow (SY) as our model donor polymer because of its exceptionally deep highest occupied molecular orbital (HOMO),[57] and make model blends with the acceptor [6,6] phenyl-C_{71}-butyric-acid-methyl ester ($PC_{71}BM$). We analyze transient photovoltage (TPV) and charge extraction (CE) experiments to

show how charge carrier recombination and densities change with SAM type under device operating conditions, and compare the kinetics of devices with different V_{OC}s. We use PA SAMs to study the effects of charge carrier recombination and V_{OC}, with the materials and device structures shown in Fig. 4.1. The energy levels are measured by ultraviolet photoelectron spectroscopy as reported in the literature (SAMs,[16] PEDOT:PSS,[16] SY,[57] $PC_{71}BM$,[113] LiF,[114] poly(3-hexylthiophene) (P3HT),[115] and [6,6]-phenyl-C_{61}-butyric acid methyl ester ($PC_{61}BM$)[115]), and the photoelectric effect (Ca and Al),[95] and the structure of Super Yellow was reported by Seo and co-workers.[94] First, we fabricate a series of bulk heterojunction (BHJ) OPV devices with the structure: ITO/modifier/Super Yellow:$PC_{71}BM$/LiF/Al (fabrication details are described in the experimental section). To study the impact of the work function of the ITO electrode on V_{OC}, we use a range of different modifiers including three SAMs: 2,6-difluorobenzylphosphonic acid (oF_2BnPA), benzylphosphonic acid (BnPA), pentafluorobenzylphosphonic acid (F_5BnPA), and the common doped conducting polymer, poly(3,4-ethylenedioxythiophene) – poly(styrenesulfonate) (PEDOT:PSS).

4.2 Transient photovoltage results and discussion

Figures 4.2a-b depict the light and dark current density versus voltage (J-V) data, respectively, for SY/$PC_{71}BM$ OPVs. In Fig. 4.2a, we observe an increase in V_{OC} that changes with the work function of the modified ITO and is consistent with previously reported data on poly(N-9′-heptadecanyl-2,7-carbazole-*alt*-5,5-(4′,7′-di-2-thienyl-2′,1′,3′-benzothiadiazole) (PCDTBT)/$PC_{71}BM$ OPVs using the same PA SAM ITO-modification procedure.[16] The dark

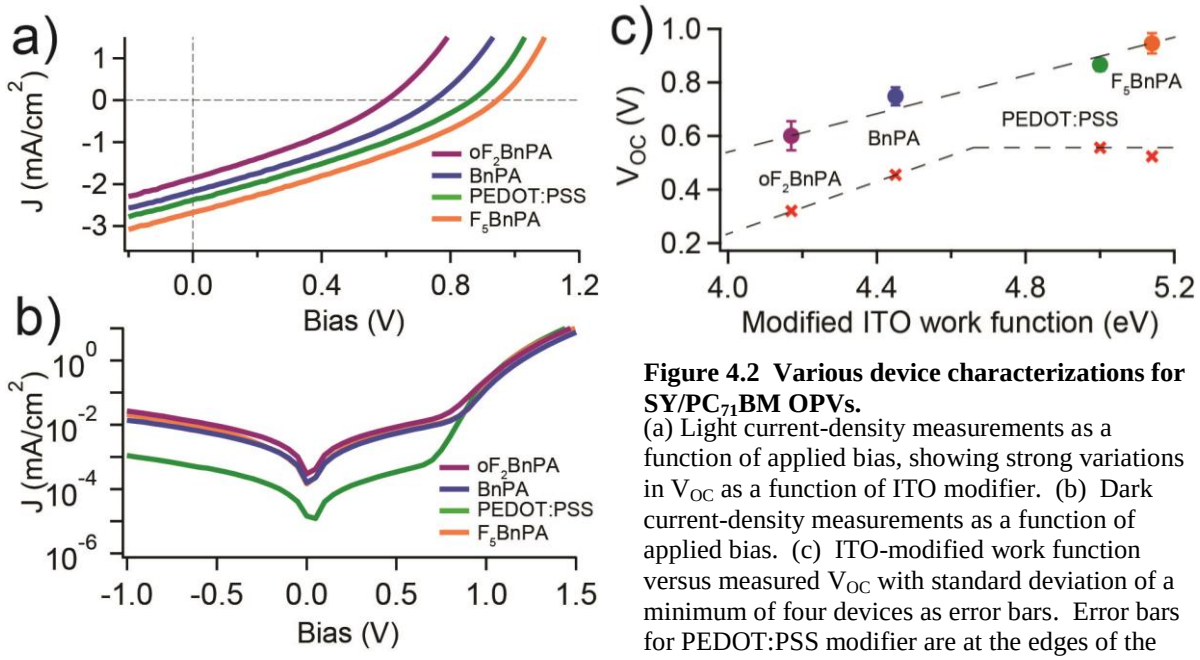

Figure 4.2 Various device characterizations for SY/$PC_{71}BM$ OPVs.
(a) Light current-density measurements as a function of applied bias, showing strong variations in V_{OC} as a function of ITO modifier. (b) Dark current-density measurements as a function of applied bias. (c) ITO-modified work function versus measured V_{OC} with standard deviation of a minimum of four devices as error bars. Error bars for PEDOT:PSS modifier are at the edges of the marker.

currents for our modified-ITO SY/$PC_{71}BM$ OPVs shown in Fig. 4.2b also show similar trends to the previously reported PCDTBT/$PC_{71}BM$ OPV data.[16]

Figure 4.2c shows V_{OC} measured under simulated AM1.5G illumination plotted against the work function of the hole extracting contact. Data for the SY/$PC_{71}BM$ SAM-modified devices are shown in the color-coded circles, and for comparison, we include V_{OC} data for SAM-modified devices fabricated with poly(3-hexylthiophene) (P3HT) and [6,6]-phenyl-C_{61}-butyric acid methyl ester ($PC_{61}BM$) (red crosses). For the P3HT/$PC_{61}BM$ we observe a linear change in V_{OC} with changing contact work function up to the P3HT HOMO (4.65 eV[115]). The deeper work function ITO-modifiers, namely PEDOT:PSS and F_5BnPA, show little change in V_{OC}, consistent with pinning to the edge of the P3HT HOMO, as has previously been reported.[57,116] Together, our data, and the results of Ratcliff and co-workers,[16] indicate that these fluorinated phosphonic acid SAMs can be used to increase the V_{OC} in bulk heterojunctions with three different active

layers, suggesting a general trend and a common mechanism. Because the range of V_{OC} modulation seems to depend on the depth of the polymer HOMO level (Fig. 4.2c), we chose SY with its unusually deep HOMO as our model polymer in order to further examine the role of the phosphonic acid SAMs on V_{OC}.

In an ideal diode, V_{OC} is generally taken to be inversely proportional to the natural logarithm of the saturation current, J_0, as shown in Equation 4.1, where n is the diode ideality factor, k is Boltzmann's constant, T is temperature in K, q is elemental charge, and J_{SC} is short-circuit current density:

Eqn. 4.1: $$V_{OC} \approx \frac{nkT}{q} \ln(\frac{J_{SC}}{J_0})$$

In the dark J-V data in Fig. 4.2b, the modifier with the largest energetic offset to the SY HOMO, oF_2BnPA, shows the largest J_0, the fastest forward current rise with applied bias, and in Fig. 4.2a the lowest V_{OC}, consistent with both Eqn. 1 and previous reports.[16,47] Notably though, the modifier with the largest V_{OC}, F_5BnPA, shows similar reverse bias dark current to the oF_2BnPA-modified device. Thus, to a first approximation, a simple analysis of the reverse dark current does not fully explain the observed trends in V_{OC} for the SAM-modified devices, consistent with the conclusion that a simple analysis of dark current parameters is insufficient to understand OPV recombination losses.[117]

We thus turn to transient photovoltage (TPV) and charge extraction (CE) to study the charge carrier recombination in these SY/PC_{71}BM OPVs under open-circuit conditions. The techniques are described in detail in chapter 2 and elsewhere,[32,35,60] and full details of our system are included in the following experimental section. Briefly, TPV uses a weak light pulse to

create a small perturbation of excess charge carriers whose recombination dynamics are measured via the transient photovoltage signal arising from the excess carrier population. An important component of these experiments is that the total background carrier density is controlled by a continuous white light bias that holds the device at a fixed charge carrier density, *n*, while the transient light pulse creates a significantly smaller change in the equilibrium carrier density, Δn. For a given device modifier, we collect these TPV voltage transients over a range of white light background intensities. We use the same white light intensities in the CE measurement to determine the charge carrier density, *n*, present in the device at each light intensity.

Figure 4.3a plots V_{OC} versus charge carrier density, *n*, (as measured via CE) across the full series of devices. The curves for the SAM devices are virtually identical, showing that the dependence of V_{OC} on charge carrier density is nearly the same for each SAM. Since the relationship between V_{OC} and *n* is determined by the quasi Fermi level splitting achieved at a given carrier density, which in turn depends on the average density of states (DOS),[118] we interpret Fig. 4.3a as an indication that the SAM treatments do not significantly affect the DOS for either electrons or holes in the devices. While we cannot completely rule out morphology changes arising from the SAMs,[53,59] the similarities between our various SAM-modified SY/PC_{71}BM blend devices thus suggest that the SAM-modification of the hole extracting contact is not significantly changing the DOS in the donor-acceptor blend. On the other hand, Fig. 4.3a shows a measurable difference between the PEDOT:PSS contact and the SAM-modified contact at low *n* ($n < 2.2 \times 10^{16}$ cm^{-3}), while all 4 materials show the same shape at high *n* ($n > 2.2 \times 10^{16}$ cm^{-3}). While the origin of the differences at low *n* are beyond the scope of the described

experiments, we speculate that they could arise from interfacial chemical reactions and interface blurring changing the DOS tail for the PEDOT:PSS-modified blend.[119]

While the V_{OC} vs. *n* plots look virtually identical, at a given charge carrier density, we

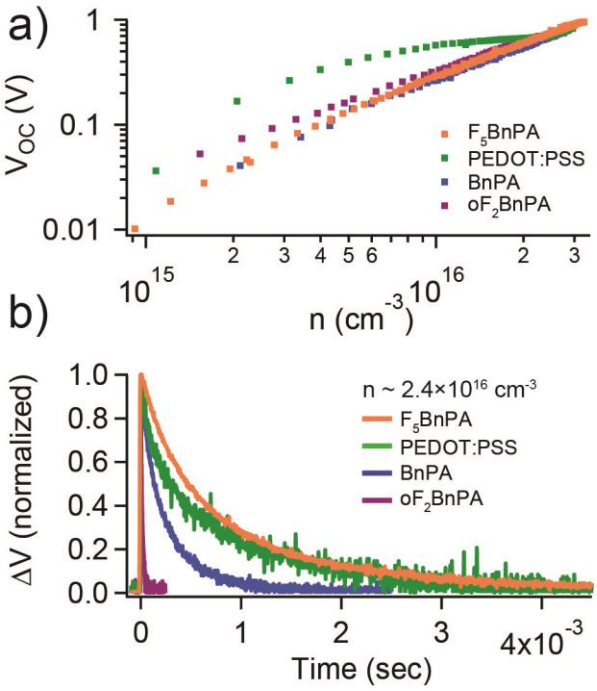

Figure 4.3 Data collected from TPV and CE experiments on SY/PC_{71}BM OPVs.
(a) V_{OC} as a function of charge carrier density (n). Strong overlap is indicative of similar density of states for all SAM-modified devices. (b) Change in voltage (ΔV) as a function of time for the four modifiers at the same charge carrier density (n=2.4x10^{16} cm^{-3}).

observe strong differences in the voltage decay time for the different SAM modifications, as shown in Figure 4.3b. In other words, while the V_{OC} obtained for each SAM at a given carrier density is identical, the light intensity required to obtain that carrier density is strongly SAM dependent because the carrier lifetime is strongly SAM dependent. For SAM-modified ITO devices with shorter voltage decay times (at fixed *n*) we observe lower V_{OC} under AM 1.5G conditions as shown in Fig. 4.2a.

While TPV data have generally been interpreted as measuring carrier recombination in the bulk of the active layer,[32,35,60] Street has suggested that TPV measures time constants reflecting recombination due to a forward diode current created by the excess photoinduced carrier population.[34] In this picture, the TPV lifetime should be "inversely proportional to the dark current at the open circuit voltage of the TPV measurement".[34] However, the implications for device performance and interface optimization are dramatically different if the forward

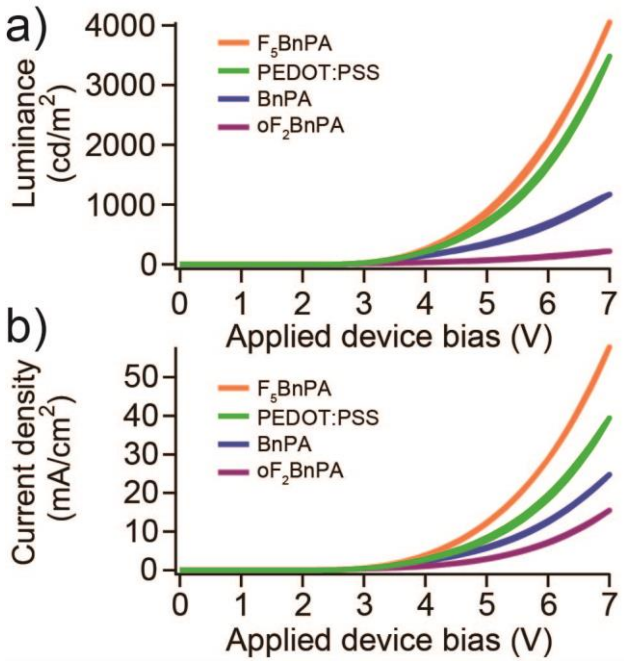

Figure 4.4 SY-only LED data for the four different ITO modifiers.
(a) Luminance versus voltage and (b) current density versus voltage both depict the trend in improved device performance when the anode modifier work function approaches the SY HOMO, thereby decreasing the injection barrier.

current is a conventional forward diode current (hole injection into the donor from ITO and electron injection into the acceptor from the Al in our devices) or is a surface recombination current made possible by the fact that both donor and acceptor domains are in contact with the

same electrode in the bulk heterojunction geometry (electrons in the acceptor recombining with holes in the donor at via ITO contact).

In an effort to distinguish between these two possibilities, we fabricated SY-only light-emitting-diodes (LEDs) using the same four ITO modifiers. LEDs are simpler systems that provide insight as to how hole injection changes as a result of ITO modification, and were fabricated with the structure shown in Fig. 4.1, with device results shown in Fig. 4.4. Fig 4.4a shows the SY-LED luminance as a function of applied device bias, and Figure 4.4b shows the current density as a function of applied bias. Both Figs. 4.4a and b suggest that oF_2BnPA has the largest hole-injection barrier of the four modifiers as it exhibits the lowest luminescent output and current density. Therefore, if TPV were measuring a conventional forward diode current (hole injection from ITO into SY), oF_2BnPA-modified devices with poor hole-injection would correspondingly show the *slowest* recombination. However, in Fig. 4.3b, we observe significantly *faster* recombination for the oF_2BnPA-modified OPV, suggesting that invoking modifier-induced changes in hole-injection at the ITO/SY interface are unable to explain the observed variations in OPV recombination.

We thus examine the possibility that the ITO-modifiers are affecting electron recombination at the ITO interface by considering how variations in the ITO work function affect interfacial band bending.[116] Regardless of the exact position of the Fermi level in the dark in the polymer/fullerene blend, as long as the modified-ITO work function lies somewhere within the semiconductor transport gap, increasing the ITO work function (bringing the ITO work function closer to the polymer HOMO) will lead to more favorable band bending at the contact. That is, a larger ITO work function will tend to create an electric field in the active

semiconductor layer that drives electrons away from the ITO/active layer interface (Fig. 4.5).[120] Consequently, recombination will be slower for electrons present in the fullerene domains at the ITO contact in the F_5BnPA-modified device.

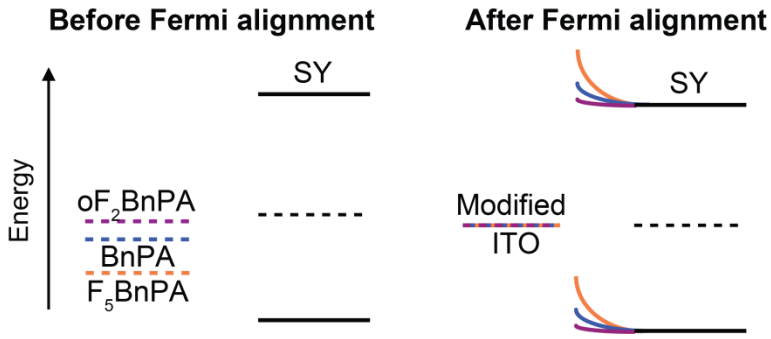

Figure 4.5 Cartoon of band bending for the PA SAMs with SY HOMO. Qualitative comparison of band bending for SY HOMO with oF_2BnPA (purple), BnPA (blue), and F_5BnPA-modified ITO (orange) before and after Fermi level alignment.

In the case of poor hole-injection between the oF_2BnPA and SY, there will be less build-up of hole density at the interface, and less-favorable band bending. Thus, there is a less-favorable electric field gradient to direct electrons away from the interface and the electrons from the $PC_{71}BM$ in contact with the ITO/oF_2BnPA/SY interface can recombine more quickly with the holes. In this context, our observed LED and OPV performance, and measured carrier lifetimes, are also consistent with previous theoretical predictions relating band bending, $V_{OC,}$ and carrier recombination .[48,49,120]

In conclusion, we show that PA SAMs modification can alter not just V_{OC}, but also carrier lifetime in bulk heterojunction OPVs. While we cannot definitively exclude the possible influence on lifetime of undetected differences in morphology, plots of V_{OC} versus carrier density are identical for all SAM-modified devices, suggesting the density of states of the active layers are not substantially altered by the SAMs. We thus hypothesize that the lifetime changes we observe are most likely the result of suppressed surface recombination of electrons in the

fullerene at the hole-extracting contact/BHJ interface in OPVs due to changes in the back surface field induced by variations in band banding at that contact.[120] We conclude that the SAMs are thus improving the selectivity of the back contact through their impact on band bending, rather than introduction of a gap in the density of states that has been suggested elsewhere for some interlayers. These results both highlight the role electrode surface recombination can play in bulk heterojunction cells, and underscore the potential to improve OPV performance by careful tailoring of interface properties such as work function[49,116] and interfacial doping.[121,122]

4.3 Experimental

1.5 cm × 1.5 cm ITO coated glass slides (TFD Inc., RMS=7±1Å) were sonicated successively in acetone and then isopropyl alcohol for 20 minutes each. Following sonication, clean slides were masked by Kapton tape for etching with HCl/Zn to create an active area strip of 0.9 cm wide ITO. Following etching the slides were rinsed and scrubbed with detergent (Micro-90) and deionized (DI) water, then rinsed in DI water and again sonicated in acetone and then isopropyl alcohol for 20 minutes each. Clean ITO slides were oxygen plasma cleaned (Harrick Plasma Cleaner PDC-32G, 18W applied) at a flow rate of 100 mL/min, typically for 6 minutes immediately prior to surface modification. Phosphonic acids (PAs) were synthesized as described in literature[57,86,97] and used to prepare 10 mM ethanolic soaking solutions. ITO substrates were soaked for 24 hours, rinsed with ethanol and blown dry with N_2 three times. Clevios P VP AI 4083 poly(3,4-ethylenedioxythiophene) -poly(styrenesulfonate) (PEDOT:PSS) was filtered through a 0.45 μm PVDF filter and briefly heated to 45°C, then spincoated (3 sec

500 RPM, 2 min 4000 RPM, 2 min 5000 RPM) in air onto freshly plasma cleaned ITO. PEDOT:PSS films were then annealed for 1 hour under N_2 flow in a custom heating stage on a 140°C hot plate, yielding 40 nm thick films as measured by a KLA Tencor Alpha Step 500 Surface Profiler. Upon surface modification completion, substrates were quickly transferred into a dry nitrogen glovebox for active layer deposition.

Super Yellow (PDY-132) was purchased from EMD Chemicals and $PC_{71}BM$ was purchased from Nano-C. Both were used as received to prepare an OPV blend of 8.4 mg SY, 26.9 mg $PC_{71}BM$ solution in 1.52 mL of anhydrous chlorobenzene in a dry nitrogen glove box (<5 ppm O_2 and <0.1 ppm H_2O, typical). The solution was allowed to spin for a minimum of 4 hours at 60°C before spincoating from warm solution. The solution was spincoated for 2 minutes at 2000 RPM to form BHJ layers that were 216 nm thick as determined by profilometry. The SY-only films were prepared similarly from a separate solution of 6.1 mg SY dissolved in 1.1 mL of chlorobenzene, with a film thickness of 83 nm.

After spincoating, devices were loaded into a glove box integrated Angstrom Engineering Åmod 600 series evaporator. 0.7 nm of LiF (LiF Anhydrous, 99.99+% metals basis, Aldrich) was thermally evaporated at a rate of 0.1 Å/sec and pressure of 3×10^{-7} Torr. This was followed by evaporation of 80 nm of aluminum (0.062" diameter Al wire, 99.999%, Lesker) at a rate of 1.5 Å/sec and pressure of 5×10^{-7} Torr.

P3HT (Reike Metals) and $PC_{61}BM$ were used as received and all device fabrication was performed in a nitrogen atmosphere glove box with anhydrous solvents. Bulk heterojuction (BHJ) films were prepared according to previous reports[123] with 40 mg/ml solutions of 1:1 P3HT:$PC_{61}BM$ by weight in 1,2-dichlorobenzene stirred at 60°C overnight for full dissolution.

Films were spincoated from room temperature solutions at 600 rpm for 60s leading to wet films that were allowed to completely dry in closed petri dishes for ~2 hours. Films were finally annealed at 150°C for 10 minutes leading to films with ~220 nm. The PV devices were completed by thermal deposition (Angstrom Evovac evaporator) of 20 nm of calcium followed by 100 nm of aluminum electrodes with an area of 11 mm^2 via a shadow mask at a base pressure of ~3×10^{-8} Torr.

A solar simulator lamp (Solar Light Co., Model XPS 400, operated by Xenon Lamp Power Supply), Keithley 2400, custom LabVIEW software, and a Si photodiode were used to collect current-voltage characteristics in a dry nitrogen glove box (<3 ppm O_2 and <0.1 ppm H_2O, typical). Luminance-voltage measurements were carried out as described previously.[14]

Transient photovoltage (TPV) and charge extraction (CE) measurements were configured after detailed literature descriptions.[32] A Royal-Blue Rebel 447.5nm LED (Luxeon Star LXML-PR01-0425) was pulsed (2 Hz, 4 μs width, 20 ns edge) by a homebuilt LED driver circuit and Agilent 33210A 10 MHz Function/Arbitrary waveform generator, and was used to generate a voltage transient measured by a Textronix TDS 2024B oscilloscope. Samples were mounted in a homebuilt vacuum chamber and tested under active vacuum (typically between 5-15 mTorr). A Bridgelux BXRA-56C9000-J white LED was controlled by custom LabVIEW software and a TTI Instruments (CPX400SA) power supply, and was used to hold the device under open-circuit conditions.

CE measurements employed a homebuilt circuit that allowed the device to be switched from open-circuit (white light on) to short-circuit (light off). The circuit employs a switch that remains open while the white light is on, and then closes when the light turns off. The function

generator sends a 10 Hz square wave to the same white LED, and the device's corresponding voltage decay transient is again measured by the oscilloscope. Post-data collection, the voltage transient is converted to a current transient using Ohm's Law, and used to determine a current volume. Charge carrier density (n) is calculated by integrating the area underneath the transient.

5 Conclusions and suggestions for future work

5.1 Conclusions

We investigated the use of PA SAMs as a means to control ITO work function and gain a deeper understanding of the device operational mechanisms. Microcontact printed phosphonic acid SAMs were shown to yield high resolution, local changes in ITO work function. The pattern fidelity was preserved and visible when used in fabrication of a patterned LED. The experiments in chapter 3 showed the ability to locally pattern the work function of ITO that could lead to possible applications in low-cost LED signage. By creating nano-to-micro-scale patterned contrast in the work function of ITO, we can locally characterize the effects using atomic force microscopy-based techniques. The successful characterization of patterned work function and subsequent LED fabrication serves as a useful model for future experiments that seek to explore differences in ITO work function and OPVs. Patterned ITO work functions also provide a means to connect local environmental changes that can be studied using atomic force microscopy to changes in large-scale device performance from larger-scale (e.g. millimeter) changes in ITO work function.

Transient photovoltage and charge extraction have been used to characterize the charge carrier recombination of PA SAM-modified OPVs. Reports in the literature emphasize the role of microstructure influencing recombination and thus V_{OC},[23] but our results discussed in Chapter 4 suggest the electrode interface can play a significant role in altering recombination. Our data suggest that certain PA SAMs may suppress surface recombination at the ITO/BHJ interface in

OPVs, leading to increases in V_{OC}. This finding further highlights the need for good energetic alignment between the electrode work functions and active layer energy levels so as to minimize surface recombination. The combination of patterned work function and atomic force microscopy-based techniques to study local changes in charge carrier recombination could connect changes in observed device performance to the local changes in work function.

The OPV community is presently pursuing replacements for ITO for a variety of reasons, including work function and cost given that indium is a rare earth metal. Though we have demonstrated that PA SAMs provide a convenient means of tuning the ITO work function, research has also shown the ability to deposit PA SAMs on alternative TCOs. With the growing interest in both oxidation resistant polymers and alternate TCOs, PA SAMs are a versatile way to adjust the TCO work function for improved energetic alignment. Furthermore, the ease and versatility of SAM processing lends itself to integration into a large scale manufacturing process.

5.2 Suggestions for future work

5.2.1 Utilities of PA SAMs

It would be interesting to investigate the effect of patterning on LED lifetimes. It is reasonable to consider that smaller regions of electroluminescence could minimize formation of hot spots of current, and thus influence luminance lifetimes. If this could be accomplished, one could envision nanoscale patterned light-emission through the use of PA SAMs to create longer-lasting macro-scale lighting effects, similar to the small dots comprising a Pointillist painting.

As mentioned previously, alternatives to ITO have been explored, yet notably, most transparent conductive oxides will inherently have work function limitations. As such, SAMs provide a means to selectively tune and control the work function, in addition to controlling film morphology,[59] surface adhesion, and wettability. Some work has already been undertaken to explore the use of PA SAMs as a means of modifying alternative transparent conductive oxide materials such as indium zinc oxide.[15] SAMs have the ability to be easily tailored to a particular application's needs, thereby reinforcing the utility of these novel materials.

5.2.2 Transient photovoltage and related experiments

It will be interesting to use TPV/TPC/CE techniques further investigate recombination and charge transport in OPVs. The transient photovoltage and photocurrent techniques have found marked success in studies of dye-sensitized solar cell studies, both in discerning recombination and also charge transport.[31,37,124,125] Notably, a review by Credgington and Durrant discussed in detail the effects of microstructure and recombination on variation in the open-circuit voltage. These variations arising from changes in morphology could be correlated to charge carrier mobility measurements, perhaps using photo-CELIV or time of flight spectroscopy.[126,127]

A difficult but rewarding direction for future TPV studies would be to attempt to correlate changes in vertical phase structure with measured changes in recombination. The studies described in this thesis (particularly chapter 4) suggest that transient techniques can be used to describe recombination that is thought to occur at the ITO/active layer interface. Some

of the literature has suggested that changes in relative concentration of polymer or fullerene in the vertical device profile is linked to changes in device performance, and furthermore hypothesized to possibly act as recombination centers in the device.[23,53,128,129] It would be exciting to show that transient techniques can be used to evaluate recombination differences that correlate to marked changes in the vertical device profile as well as device performance.

For example, within a particular polymer/fullerene OPV blend system, it would be interesting to control the ITO surface energy and evaluate whether or not the changes in device performance correlate to differences in recombination. Bulliard and co-workers describe the use of SAMs to control surface energy while maintaining a constant work function,[76] and a similar approach could be used to unambiguously evaluate differences in recombination as a result of varied surface energetics and composition.

Additionally, charge recombination at the interface could be investigated with respect to the charge selectivity of the contact. Blocking layers have been suggested for use in OPVs to suppress diffusion and reaction at the electrode/active-layer interface,[20,49] as well as to improve electronic equilibrium in the devices.[130] Thus, an interesting follow-up study to chapter 4 would be to examine more fully the effects of contact-selectivity, for example comparing ITO modifiers with a similar work function, e.g. F_5BnPA, PEDOT:PSS, and NiOx, a hole-selective interlayer.[130,131] These example materials exhibit similar work functions on ITO, but differ in their ability to block undesired carriers and thus may show differences in surface recombination.

Appendices

Appendix A Igor Pro procedure files used to process data.

Each of the Igor Pro procedure files contain significant comments that further describe each of the individual variables and overall goals of the procedure.

Type	Procedure file (.ipf)	Function	Notes
TPV	Load_OE_Files5 alpha	LoadTPV(keyword, x1, x2)	Most recent single pixel testing. Assumes "standard device architecture" – i.e. that voltage measured on the scope is positive.
TPV	Load_OE_Files5 beta	LoadTPV(keyword, x1, x2)	Assumes "standard device architecture" – i.e. that voltage measured on the scope is positive.
CE	Load_OE_Files5 alpha	LoadCE(keyword, x1,x2, nmthick, posit)	Most recent single pixel testing. Assumes "standard device architecture" – i.e. that voltage measured on the scope is positive.
CE	Load_OE_Files5 beta	LoadCE(keyword, x1,x2, nmthick, pix, posit)	Pix refers to number of pixels on a substrate that are connected together. Applicable to e.g. Super Yellow-based OPVs because pixels may be connected to increase the total current output. Acts as a multiplier for the total device area (one pixel area is 0.0386 cm^2, and thus a pix of 3 would set the device area to 0.0386 cm^2*3 = 0.1158 cm^2). Relevant for low-current output devices that need to incorporate device areas other than 1 pixel. Assumes "standard device architecture" – i.e. that voltage measured on the scope is positive.
CE	Load_OE_Files5 beta_mask	LoadCE(keyword, x1,x2, nmthick, pix, posit)	Same as OE_Files5 beta, but accounts for new mask area (0.0136 cm^2).

Table A 1 Descriptions of the TPV and CE Igor Pro Procedure files available for data processing.

The predominant change in advancing from "Load_OE_Files5 beta" to "Load_OE_Files5 beta_mask" is the incorporation of the device masked pixel area (0.0136 cm^2) as the nominal

device area instead of the entire (unmasked) device area (0.0386 cm^2). Other cosmetic improvements were also made between procedure file versions that do not affect numeric calculations.

Historical note: "Load_OE_Files5 beta" was written prior to the addition of the unity gain buffer (UGB) into the instrument set-up (described in Chapter 2.3.1). Given the previous inconsistencies in measuring V_{OC} prior to the UGB, the "pix" variable in the Igor Pro procedure was a simple way to account for simultaneous measurement of multiple devices.

Appendix B Notes about data processing and Igor Pro wave-naming scheme in charge extraction data-processing procedures.

General notes and assumptions for Igor Pro data processing procedures

- I assume the TPV data includes a repeated measurement of the 0V on the DAQ (no CW white light). In practice, this serves as a good "sanity check" to ensure device stability before and after testing a series of white light intensities. (For advanced Igor users: Specifically the TPV tau wave data is copied into the CE data folder. The first data point (point 0) from the copied tau wave is deleted since only 1 CE measurement is acquired in the dark. This is done to simplify the (code writing for) plotting of tau versus n.
- Throughout my procedure files, I name things "tau" when they actually are equivalent to what is called $\tau_{\Delta n}$ in the (Maurano/Shuttle/Durrant) literature (see Chapter 2.3.1).
- In the TPV data work-up, "Krec" is simply calculated as 1/tau. No attempts have been made to correct or account for differences in *n*, as suggested to be necessary in the literature (Maurano/Shuttle/Durrant).

Process TPV Data (Igor Pro – Procedures require v6 or higher)

All described procedure files are stored both on the TPV computer, as well as the Ginger server. On the TPV computer, the (e.g) procedure files are stored:

C:→ Data→Kris→Load_OE_files5Alpha.ipf (.ipf = igor procedure file)

Note to experienced Igor users: All x and y data are loaded as separate waves. There is no "built-in" spacing to the y wave data points. All data plots subsequently require both the y wave data and its corresponding x wave data in order to display properly.

Outline of data processing steps and helpful hints

- Create two separate folders for the data, one each for TPV and for CE, abiding by the following naming conventions:
    - Igor Pro requires folder names to start with a letter (note, raw data file names should also begin with a letter).

- Folder names can be whatever you want as long as they are paired, differing only by their suffix "_TPV" or "_CE".
  - E.g.
    - P3HT_5p5_TPV
    - P3HT_5p5_CE

- Select the TPV folder by either dragging the big red arrow to the folder name, or right clicking on the folder name and selecting "Set Current Data Folder". The "Current Data Folder:" box at the top of the data browser should now read "root:YourFolderName_TPV:".
- Load TPV data using the command window (CTRL J to bring command window forward): Type in function and press enter to execute:
  - LoadTPV(keyword, x1, x2)
    - Keyword: e.g. "TPV" (an identifier for finding file name in the folder; must be in quotes because Igor expects a string). Keyword is the root file name for the data you wish to load. Igor will later prompt you to specify a folder to browse for data.
    - x1 and x2: Denote the amount of baseline used to normalize data. Igor expects points (not x values). These points will be the start/stop points for averaging to determine the device V_{OC}. Choose points that stay away from the rising edge of your transient photovoltage peak. The screen of the oscilloscope has 2500 pts. Therefore, when position=0 on the scope that is at point 1250. A typical baseline will be something like 50-650 pts, therefore x1=50 and x2=650. These numbers are again specific to each experiment depending on where the position of the peak is located, but should incorporate enough baseline to make a meaningful measurement of V_{OC}.
      - "Load_OE_files5Alpha.ipf" and earlier versions of Kristina's code do not have code written to adjust the position of the TPV data. The function assumes that all TPV data is collected at position = 0.
    - Example of command run in Igor:
      LoadTPV("TPV", 50, 650)

- After executing the Load function you will be prompted to change the symbolic path. Click "Yes" and then "Browse" to find the folder containing your TPV data.
- Two plots will pop up. The first will be the raw data and the second is the normalized data. You will want to fit a single exponential function to the normalized data. To do this to all curves on the graph at once, make sure this graph is selected. Then go to the command window and enter the function, "sglexpfit()". Press enter and more plots will appear!
- Note: If your data seem "off" (↑light intensity is not corresponding to ↓tau values) it is possible that the single exponential function did not correctly fit your data. To do a fit by hand go to the normalized plot. Zoom in to double check the fit (red lines). If the fit is off, use the cursors to choose new start and end points for the fit. Right click on the dark circle in the bottom left hand corner of the plot to select the wave being

fitted. Select "Analysis" from the menu, then "Quick Fit" → "exp_xoffset". You can check the command window to see how the new fit compares. If the fit was successful, Igor will state, "fit converged properly". Compare the output "tau" values of the old and new fits. If the new fit is better, the new data must be manually entered into the table (i.e. change the data point in the wave). This is important because the TPV data will be used for the charge extraction plots (described later).

- There is also a function that performs double exponential (instead of single exponential) fits. It can be executed with the command "dblexpfit()". In some cases a double exponential may provide a better fit to the data.
- Before saving plots and tables make sure all waves are stored in their proper folder and labeled correctly. Save a graph recreation macro by clicking once on the "X" and giving it a unique name (starting with a letter). These graph macros can be accessed either via the command window (graphname()) or from the menus: Windows\Graph Macros. Saving table recreation macros is similar.

Overview of CE calculation steps

Each subsequent calculation performed on the raw CE data generates a new wave with a suffix pertaining to the calculation performed. For example, as raw voltage data is converted to a current using Ohm's law, the original y wave data (e.g. CEb14p2_0_40V) is used to populate a new wave of current data (CEb14p2_0_40V_c). Each newly generated wave is plotted with the appropriate corresponding x (time) data and is summarized below.

The x data is eventually corrected so that the position of the peak decay shows at t=0 seconds. This is achieved by simply adding the position value to each of the values in the wave of x data. The new "zeroed" data is denoted by the addition of a "z" to the wave name (CE14p2_0_40V_x to CE14p2_0_40V_xz).

Table B.1 lists the graphs made when charge extraction data is loaded into Igor, beginning on the bottom of the stack of graphs that are generated. An example wave name and its subsequently calculated waves are included. All data are plotted against the corresponding x data (e.g. CE14p2_0_40V_x) except as noted.

Example wave name	Plot contents	Plot axes
CE14p2_0_40V	Raw oscilloscope data (Volts)	voltage vs. time
CE14p2_0_40V_c	Current (Amps) calculated from Ohm's Law	current vs. time
CE14p2_0_40V_J	Current density (current divided by device area)	current density vs. time
CE14p2_0_40V_Y	Current volume (current density divided by device thickness)	current volume vs. time
CE14p2_0_40V_Y CE14p2_0_40V_xz	Corrected current volume (current density divided by device thickness)	current volume vs. zeroed time
CE14p2_0_40V_YzS CE14p2_0_40V_xz	Corrected current volume (current density divided by device thickness); data prior to t=0 deleted	current volume vs. zeroed time; data prior to t=0 deleted

Table B 1 Description of CE wave naming scheme and related auto-generated plots in Igor Pro.

It is recommended to acquire a "background" set of CE measurements at each light intensity with the device shielded from illumination and all of the circuitry in place. By repeating the CE measurements "in the dark" and then subtracting them from the actual data, we strive to minimize any circuit artifacts our reported data.

- After loading both the background and the charge extraction data into the same CE data folder (thus running the "LoadCE" function once for the raw data and once again for the background data; refer to Appendix A for details on running procedure functions), the background must be subtracted. In each instance, the "_YzS" data will need to be subtracted. As the waves were created, two text waves containing the y and x list of the wave names in the "_YzS vs _xz" data are generated as a way of quickly subtracting and plotting the appropriate data. Y data will be populated in the wave beginning "CEYzS", while x data will be in "CEXzS". A number will be affixed to the end of the text wave list, beginning with 0, to prevent data from being overwritten. In this way, it does not matter what order the raw CE data and the background CE data were loaded into Igor, as long as each can be identified.
    - E.g. After loading both background and real CE data, the following text waves (containing the "_YzS" or "_xz" wave names) will be generated: CEYzS0, CEYzS1, CEXz0, CEXz1.
- Run the background subtraction function in order to subtract the data and plot the newly calculated difference spectra versus zeroed x data.
    - Bckgrd_Sub(big, small, xdata)
        - big: the real CE data (bigger numbers)
        - small: the background CE data (smaller numbers)

        - xdata: name of the x wave against which the difference will be plotted
    - Example of command run in Igor (if background CE was loaded in first, the background y data is in CEYzS0 because it was the first text wave to be written):
        - Bckgrd_Sub(CEYzS1, CEYzS0, CEXz1)
            - Both the background and real CE data should have the same x data because the timebase and position are the same; thus, it does not matter whether e.g. CEXz1 or CEXz0 is selected for the command.
- After the difference spectra are generated, the data need to be integrated. Much as the single exponential fits were performed all at once to the plotted TPV data, the integration will be performed all at once on the difference plot using the Int_N() function.
    - Int_N()
        - The function will be executed on the top-most graph, and will generate a few different plots.
    - Note: the "Calc_N()" function is obsolete – it should give a very similar answer to Int_N() but instead of integrating it uses Igor's "AreaXY" function that "integrates" using a trapezoidal area calculation. See Igor's help file for "AreaXY" for more info.

References

(1) Green, M. A.; Emery, K.; Hishikawa, Y.; Warta, W.; Dunlop, E. D. *Prog. Photovoltaics* **2013**, *21*, 1.
(2) You, J. B.; Dou, L. T.; Yoshimura, K.; Kato, T.; Ohya, K.; Moriarty, T.; Emery, K.; Chen, C. C.; Gao, J.; Li, G.; Yang, Y. *Nat. Commun.* **2013**, *4*, 1446.
(3) Krebs, F. C.; Tromholt, T.; Jorgensen, M. *Nanoscale* **2010**, *2*, 873.
(4) Feldman, D.; Barbose, G.; Margolis, R.; Wiser, R.; Darghouth, N.; Goodrich, A. *Photovoltaic (PV) Pricing Trends: Historical, Recent, and Near-Term Projections*, **2012**.
(5) Brabec, C. J. *Sol. Energy Mater.* **2004**, *83*, 273.
(6) *Organic photovoltaics : materials, device physics, and manufacturing technologies*; Wiley-VCH: Weinheim, **2008**.
(7) Chamberlain, G. A. *Sol Cells* **1983**, *8*, 47.
(8) Tang, C. W. *Appl. Phys. Lett.* **1986**, *48*, 183.
(9) Yu, G.; Gao, J.; Hummelen, J. C.; Wudl, F.; Heeger, A. J. *Science* **1995**, *270*, 1789.
(10) Halls, J. J. M.; Walsh, C. A.; Greenham, N. C.; Marseglia, E. A.; Friend, R. H.; Moratti, S. C.; Holmes, A. B. *Nature* **1995**, *376*, 498.
(11) Yu, G.; Heeger, A. J. *J. Appl. Phys.* **1995**, *78*, 4510.
(12) Kippelen, B.; Brédas, J.-L. *Energy Environ. Sci.* **2009**, *2*, 251.
(13) Yip, H. L.; Jen, A. K. Y. *Energy Environ. Sci.* **2012**, *5*, 5994.
(14) Knesting, K. M.; Hotchkiss, P. J.; MacLeod, B. A.; Marder, S. R.; Ginger, D. S. *Adv. Mater.* **2012**, *24*, 642.
(15) Bulusu, A.; Paniagua, S. A.; MacLeod, B. A.; Sigdel, A. K.; Berry, J. J.; Olson, D. C.; Marder, S. R.; Graham, S. *Langmuir* **2013**, *29*, 3935.
(16) Ratcliff, E. L.; Garcia, A.; Paniagua, S. A.; Cowan, S. R.; Giordano, A. J.; Ginley, D. S.; Marder, S. R.; Berry, J. J.; Olson, D. C. *Adv. Energy Mater.* **2013**, *3*, 647.
(17) Love, J. C.; Estroff, L. A.; Kriebel, J. K.; Nuzzo, R. G.; Whitesides, G. M. *Chem. Rev.* **2005**, *105*, 1103.
(18) Ulman, A. *Chem. Rev.* **1996**, *96*, 1533.
(19) Hotchkiss, P. J.; Jones, S. C.; Paniagua, S. A.; Sharma, A.; Kippelen, B.; Armstrong, N. R.; Marder, S. R. *Acc. Chem. Res.* **2012**, *45*, 337.
(20) Chen, L. M.; Xu, Z.; Hong, Z. R.; Yang, Y. *J. Mater. Chem.* **2010**, *20*, 2575.
(21) Chen, S.; Manders, J.; Tsang, S. W.; So, F. *J. Mater. Chem.* **2012**, *22*, 24202.
(22) Smith, R. K.; Lewis, P. A.; Weiss, P. S. *Prog. Surf. Sci.* **2004**, *75*, 1.
(23) Credgington, D.; Durrant, J. R. *J. Phys. Chem. Lett.* **2012**, *3*, 1465.
(24) Clarke, T. M.; Durrant, J. R. *Chem. Rev.* **2010**, *110*, 6736.
(25) Gao, F.; Wang, J. P.; Blakesley, J. C.; Hwang, I. C.; Li, Z.; Greenham, N. C. *Adv. Energy Mater.* **2012**, *2*, 956.
(26) Schlenker, C. W.; Thompson, M. E. *Chem. Commun.* **2011**, *47*, 3702.
(27) Boix, P. P.; Ajuria, J.; Pacios, R.; Garcia-Belmonte, G. *J. Appl. Phys.* **2011**, *109*, 074514.

(28) Fabregat-Santiago, F.; Garcia-Belmonte, G.; Mora-Sero, I.; Bisquert, J. *Phys. Chem. Chem. Phys.* **2011**, *13*, 9083.
(29) Garcia-Belmonte, G.; Munar, A.; Barea, E. M.; Bisquert, J.; Ugarte, I.; Pacios, R. *Org. Electron.* **2008**, *9*, 847.
(30) Mozer, A. J.; Sariciftci, N. S.; Lutsen, L.; Vanderzande, D.; Osterbacka, R.; Westerling, M.; Juska, G. *Appl. Phys. Lett.* **2005**, *86*, 112104.
(31) O'Regan, B. C.; Bakker, K.; Kroeze, J.; Smit, H.; Sommeling, P.; Durrant, J. R. *J. Phys. Chem. B* **2006**, *110*, 17155.
(32) Maurano, A.; Shuttle, C. C.; Hamilton, R.; Ballantyne, A. M.; Nelson, J.; Zhang, W. M.; Heeney, M.; Durrant, J. R. *J. Phys. Chem. C* **2011**, *115*, 5947.
(33) Cowan, S. R.; Street, R. A.; Cho, S.; Heeger, A. J. *Phys. Rev. B* **2011**, *83*, 035205.
(34) Street, R. A. *Phys. Rev. B* **2011**, *84*, 075208.
(35) Shuttle, C. G.; Maurano, A.; Hamilton, R.; O'Regan, B.; de Mello, J. C.; Durrant, J. R. *Appl. Phys. Lett.* **2008**, *93*, 183501.
(36) Shuttle, C. G.; Hamilton, R.; O'Regan, B. C.; Nelson, J.; Durrant, J. R. *Proc. Natl. Acad. Sci. U. S. A.* **2010**, *107*, 16448.
(37) O'Regan, B. C.; Lopez-Duarte, I.; Martinez-Diaz, M. V.; Forneli, A.; Albero, J.; Morandeira, A.; Palomares, E.; Torres, T.; Durrant, J. R. *J. Am. Chem. Soc.* **2008**, *130*, 2906.
(38) Hamilton, R.; Shuttle, C. G.; O'Regan, B.; Hammant, T. C.; Nelson, J.; Durrant, J. R. *J. Phys. Chem. Lett.* **2010**, *1*, 1432.
(39) Chen, S.; Small, C. E.; Amb, C. M.; Subbiah, J.; Lai, T. H.; Tsang, S. W.; Manders, J. R.; Reynolds, J. R.; So, F. *Adv. Energy Mater.* **2012**, *2*, 1333.
(40) Byers, J. C.; Ballantyne, S.; Rodionov, K.; Mann, A.; Semenikhin, O. A. *ACS Appl. Mater. Interfaces* **2011**, *3*, 392.
(41) Bisquert, J.; Garcia-Belmonte, G. *J. Phys. Chem. Lett.* **2011**, *2*, 1950.
(42) Garcia-Belmonte, G.; Bisquert, J. *Appl. Phys. Lett.* **2010**, *96*, 3.
(43) Street, R. A.; Schoendorf, M. *Phys. Rev. B* **2010**, *81*, 205307
(44) Hawks, S. A.; Deledalle, F.; Yao, J.; Rebois, D. G.; Li, G.; Nelson, J.; Yang, Y.; Kirchartz, T.; Durrant, J. R. *Adv. Energy Mater.* **2013**, *3*, 1201.
(45) Li, Z.; McNeill, C. R. *J. Appl. Phys.* **2011**, *109*, 7.
(46) Tada, A.; Geng, Y. F.; Nakamura, M.; Wei, Q. S.; Hashimoto, K.; Tajima, K. *Phys. Chem. Chem. Phys.* **2012**, *14*, 3713.
(47) Goh, C.; Scully, S. R.; McGehee, M. D. *J. Appl. Phys.* **2007**, *101*, 114503.
(48) Tress, W.; Leo, K.; Riede, M. *Adv. Funct. Mater.* **2011**, *21*, 2140.
(49) Tress, W.; Leo, K.; Riede, M. *Phys. Rev. B* **2012**, *85*, 155201.
(50) Hains, A. W.; Liu, J.; Martinson, A. B. F.; Irwin, M. D.; Marks, T. J. *Adv. Funct. Mater.* **2010**, *20*, 595.
(51) Hau, S. K.; Cheng, Y. J.; Yip, H. L.; Zhang, Y.; Ma, H.; Jen, A. K. Y. *ACS Appl. Mater. Interfaces* **2010**, *2*, 1892.
(52) Lin, Y. Y.; Lee, Y. Y.; Chang, L. W.; Wu, J. J.; Chen, C. W. *Appl. Phys. Lett.* **2009**, *94*, 063308.

(53) Mauger, S. A.; Chang, L.; Friedrich, S.; Rochester, C. W.; Huang, D. M.; Wang, P.; Moule, A. J. *Adv. Funct. Mater.* **2013**, *23*, 1935.
(54) Kim, Y. S.; Kim, T.; Kim, B.; Lee, D. K.; Kim, H.; Ju, B. K.; Kim, K. *Org. Electron.* **2013**, *14*, 1749.
(55) Gliboff, M.; Sang, L. Z.; Knesting, K. M.; Schalnat, M. C.; Mudalige, A.; Ratcliff, E. L.; Li, H.; Sigdel, A. K.; Giordano, A. J.; Berry, J. J.; Nordlund, D.; Seidler, G. T.; Brédas, J. L.; Marder, S. R.; Pemberton, J. E.; Ginger, D. S. *Langmuir* **2013**, *29*, 2166.
(56) Tillack, A. F.; Noone, K. M.; MacLeod, B. A.; Nordlund, D.; Nagle, K. P.; Bradley, J. A.; Hau, S. K.; Yip, H. L.; Jen, A. K. Y.; Seidler, G. T.; Ginger, D. S. *ACS Appl. Mater. Interfaces* **2011**, *3*, 726.
(57) MacLeod, B. A.; Horwitz, N. E.; Ratcliff, E. L.; Jenkins, J. L.; Armstrong, N. R.; Giordano, A. J.; Hotchkiss, P. J.; Marder, S. R.; Campbell, C. T.; Ginger, D. S. *J. Phys. Chem. Lett.* **2012**, *3*, 1202.
(58) Xia, Y. N.; Whitesides, G. M. *Angew. Chem. Int. Ed.* **1998**, *37*, 551.
(59) Park, L. Y.; Munro, A. M.; Ginger, D. S. *J. Am. Chem. Soc.* **2008**, *130*, 15916.
(60) Maurano, A.; Hamilton, R.; Shuttle, C. G.; Ballantyne, A. M.; Nelson, J.; O'Regan, B.; Zhang, W. M.; McCulloch, I.; Azimi, H.; Morana, M.; Brabec, C. J.; Durrant, J. R. *Adv. Mater.* **2010**, *22*, 4987.
(61) Shuttle, C. G.; O'Regan, B.; Ballantyne, A. M.; Nelson, J.; Bradley, D. D. C.; Durrant, J. R. *Phys. Rev. B* **2008**, *78*, 113201.
(62) Barnes, P. R. F.; Miettunen, K.; Li, X.; Anderson, A. Y.; Bessho, T.; Gratzel, M.; O'Regan, B. C. *Adv. Mater.* **2013**, *25*, 1881.
(63) Li, L.-L.; Chang, Y.-C.; Wu, H.-P.; Diau, E. W.-G. *Int. Rev. Phys. Chem.* **2012**, *31*, 420.
(64) Fichet, G.; Corcoran, N.; Ho, P. K. H.; Arias, A. C.; MacKenzie, J. D.; Huck, W. T. S.; Friend, R. H. *Adv. Mater.* **2004**, *16*, 1908.
(65) Yim, K. H.; Zheng, Z. J.; Friend, R. H.; Huck, W. T. S.; Kim, J. S. *Adv. Funct. Mater.* **2008**, *18*, 2897.
(66) Brondijk, J. J.; Li, X.; Akkerman, H. B.; Blom, P. W. M.; de Boer, B. *Appl. Phys. A: Mater. Sci. Process.* **2009**, *95*, 1.
(67) Wu, K. Y.; Yu, S. Y.; Tao, Y. T. *Langmuir* **2009**, *25*, 6232.
(68) Mathijssen, S. G. J.; van Hal, P. A.; van den Biggelaar, T. J. M.; Smits, E. C. P.; de Boer, B.; Kemerink, M.; Janssen, R. A.; de Leeuw, D. M. *Adv. Mater.* **2008**, *20*, 2703.
(69) Gundlach, D. J.; Royer, J. E.; Park, S. K.; Subramanian, S.; Jurchescu, O. D.; Hamadani, B. H.; Moad, A. J.; Kline, R. J.; Teague, L. C.; Kirillov, O.; Richter, C. A.; Kushmerick, J. G.; Richter, L. J.; Parkin, S. R.; Jackson, T. N.; Anthony, J. E. *Nat. Mater.* **2008**, *7*, 216.
(70) Noh, Y. Y.; Cheng, X. Y.; Tello, M.; Lee, M. J.; Sirringhaus, H. *Semicond. Sci. Technol.* **2011**, *26*, 034003.
(71) Jia, Z.; Lee, V. W.; Kymissis, I.; Floreano, L.; Verdini, A.; Cossaro, A.; Morgante, A. *Phys. Rev. B* **2010**, *82*, 125457.
(72) Vyklicky, L.; Afzali-Ardakani, A.; Kagan, C. R. *Langmuir* **2005**, *21*, 11574.
(73) Zuppiroli, L.; Si-Ahmed, L.; Kamaras, K.; Nuesch, F.; Bussac, M. N.; Ades, D.; Siove, A.; Moons, E.; Gratzel, M. *Eur. Phys. J. B* **1999**, *11*, 505.

(74) Ling, I. M.; Chen, L. H. *Curr. Appl Phys.* **2010**, *10*, 346.
(75) Mori, T.; Nishino, S.; Nishikawa, T.; Ogawa, S. *Jpn. J. Appl. Phys.* **2008**, *47*, 455.
(76) Bulliard, X.; Ihn, S. G.; Yun, S.; Kim, Y.; Choi, D.; Choi, J. Y.; Kim, M.; Sim, M.; Park, J. H.; Choi, W.; Cho, K. *Adv. Funct. Mater.* **2010**, *20*, 4381.
(77) Zschieschang, U.; Halik, M.; Klauk, H. *Langmuir* **2008**, *24*, 1665.
(78) Gomez, E. D.; Loo, Y. L. *J. Mater. Chem.* **2010**, *20*, 6604.
(79) Miao, Q.; Lefenfeld, M.; Nguyen, T. Q.; Siegrist, T.; Kloc, C.; Nuckolls, C. *Adv. Mater.* **2005**, *17*, 407.
(80) Virkar, A. A.; Mannsfeld, S.; Bao, Z. A.; Stingelin, N. *Adv. Mater.* **2010**, *22*, 3857.
(81) Koide, Y.; Such, M. W.; Basu, R.; Evmenenko, G.; Cui, J.; Dutta, P.; Hersam, M. C.; Marks, T. J. *Langmuir* **2003**, *19*, 86.
(82) Koide, Y.; Wang, Q. W.; Cui, J.; Benson, D. D.; Marks, T. J. *J. Am. Chem. Soc.* **2000**, *122*, 11266.
(83) Bardecker, J. A.; Ma, H.; Kim, T.; Huang, F.; Liu, M. S.; Cheng, Y. J.; Ting, G.; Jen, A. K. Y. *Adv. Funct. Mater.* **2008**, *18*, 3964.
(84) Sharma, A.; Haldi, A.; Hotchkiss, P. J.; Marder, S. R.; Kippelen, B. *J. Appl. Phys.* **2009**, *105*, 074511.
(85) Pechy, P.; Rotzinger, F. P.; Nazeeruddin, M. K.; Kohle, O.; Zakeeruddin, S. M.; Humphrybaker, R.; Gratzel, M. *J. Chem. Soc., Chem. Commun.* **1995**, 65.
(86) Sharma, A.; Hotchkiss, P. J.; Marder, S. R.; Kippelen, B. *J. Appl. Phys.* **2009**, *105*, 084507.
(87) Appleyard, S. F. J.; Day, S. R.; Pickford, R. D.; Willis, M. R. *J. Mater. Chem.* **2000**, *10*, 169.
(88) Appleyard, S. F. J.; Willis, M. R. *Opt. Mater.* **1998**, *9*, 120.
(89) Besbes, S.; Ltaief, A.; Reybier, K.; Ponsonnet, L.; Jaffrezic, N.; Davenas, J.; Ben Ouada, H. *Synth. Met.* **2003**, *138*, 197.
(90) Watanabe, T.; Fujihira, M. *Ultramicroscopy* **2009**, *109*, 1035.
(91) Ganzorig, C.; Kwak, K. J.; Yagi, K.; Fujihira, M. *Appl. Phys. Lett.* **2001**, *79*, 272.
(92) Ganzorig, C.; Sakomura, M.; Ueda, K.; Fujihira, M. *Appl. Phys. Lett.* **2006**, *89*, 263501.
(93) Paniagua, S. A.; Hotchkiss, P. J.; Jones, S. C.; Marder, S. R.; Mudalige, A.; Marrikar, F. S.; Pemberton, J. E.; Armstrong, N. R. *J. Phys. Chem. C* **2008**, *112*, 7809.
(94) Seo, J. H.; Namdas, E. B.; Gutacker, A.; Heeger, A. J.; Bazan, G. C. *Appl. Phys. Lett.* **2010**, *97*, 043303.
(95) In *91st Edition (Internet Version 2011)*; Haynes, W. M., Ed.; CRC Press/Taylor and Francis, Boca Raton, FL: **2011**.
(96) Paramonov, P. B.; Paniagua, S. A.; Hotchkiss, P. J.; Jones, S. C.; Armstrong, N. R.; Marder, S. R.; Brédas, J. L. *Chem. Mater.* **2008**, *20*, 5131.
(97) Hotchkiss, P. J.; Li, H.; Paramonov, P. B.; Paniagua, S. A.; Jones, S. C.; Armstrong, N. R.; Brédas, J. L.; Marder, S. R. *Adv. Mater.* **2009**, *21*, 4496.
(98) Li, H.; Paramonov, P.; Brédas, J. L. *J. Mater. Chem.* **2010**, *20*, 2630.
(99) Gong, X.; Moses, D.; Heeger, A. J.; Liu, S.; Jen, A. K. Y. *Appl. Phys. Lett.* **2003**, *83*, 183.
(100) Sheats, J. R.; Roitman, D. B. *Synth. Met.* **1998**, *95*, 79.
(101) Aziz, H.; Popovic, Z. D. *Chem. Mater.* **2004**, *16*, 4522.

(102) Doubina, N.; Paniagua, S. A.; Soldatova, A. V.; Jen, A. K. Y.; Marder, S. R.; Luscombe, C. K. *Macromolecules* **2011**, *44*, 512.
(103) Berry, J. J.; Widjonarko, N. E.; Bailey, B. A.; Sigdel, A. K.; Ginley, D. S.; Olson, D. C. *IEEE J. Sel. Top. Quantum Electron.* **2010**, *16*, 1649.
(104) Wei, J. H.; Coffey, D. C.; Ginger, D. S. *J. Phys. Chem. B* **2006**, *110*, 24324.
(105) Coffey, D. C.; Ginger, D. S. *J. Am. Chem. Soc.* **2005**, *127*, 4564.
(106) Pingree, L. S. C.; Reid, O. G.; Ginger, D. S. *Adv. Mater.* **2009**, *21*, 19.
(107) He, Z. C.; Zhong, C. M.; Su, S. J.; Xu, M.; Wu, H. B.; Cao, Y. *Nat. Photonics* **2012**, *6*, 591.
(108) Forrest, S. R. *MRS Bull.* **2005**, *30*, 28.
(109) Shaheen, S. E.; Ginley, D. S.; Jabbour, G. E. *MRS Bull.* **2005**, *30*, 10.
(110) Servaites, J. D.; Ratner, M. A.; Marks, T. J. *Energy Environ. Sci.* **2011**, *4*, 4410.
(111) Ren, G. Q.; Schlenker, C. W.; Ahmed, E.; Subramaniyan, S.; Olthof, S.; Kahn, A.; Ginger, D. S.; Jenekhe, S. A. *Adv. Funct. Mater.* **2013**, *23*, 1238.
(112) Dou, L. T.; You, J. B.; Yang, J.; Chen, C. C.; He, Y. J.; Murase, S.; Moriarty, T.; Emery, K.; Li, G.; Yang, Y. *Nat. Photonics* **2012**, *6*, 180.
(113) Walker, B.; Tomayo, A. B.; Dang, X. D.; Zalar, P.; Seo, J. H.; Garcia, A.; Tantiwiwat, M.; Nguyen, T. Q. *Adv. Funct. Mater.* **2009**, *19*, 3063.
(114) Shaheen, S. E.; Jabbour, G. E.; Morrell, M. M.; Kawabe, Y.; Kippelen, B.; Peyghambarian, N.; Nabor, M. F.; Schlaf, R.; Mash, E. A.; Armstrong, N. R. *J. Appl. Phys.* **1998**, *84*, 2324.
(115) Guan, Z. L.; Kim, J. B.; Wang, H.; Jaye, C.; Fischer, D. A.; Loo, Y. L.; Kahn, A. *Org. Electron.* **2010**, *11*, 1779.
(116) Hwang, J.; Wan, A.; Kahn, A. *Mater. Sci. Eng., R* **2009**, *64*, 1.
(117) Kirchartz, T.; Deledalle, F.; Tuladhar, P. S.; Durrant, J. R.; Nelson, J. *J. Phys. Chem. Lett.* **2013**, *4*, 2371.
(118) Garcia-Belmonte, G.; Boix, P. P.; Bisquert, J.; Lenes, M.; Bolink, H. J.; La Rosa, A.; Filippone, S.; Martin, N. *J. Phys. Chem. Lett.* **2010**, *1*, 2566.
(119) Huang, D. M.; Mauger, S. A.; Friedrich, S.; George, S. J.; Dumitriu-LaGrange, D.; Yoon, S.; Moule, A. J. *Adv. Funct. Mater.* **2011**, *21*, 1657.
(120) Blakesley, J. C.; Neher, D. *Phys. Rev. B* **2011**, *84*, 075210
(121) Qi, Y. B.; Sajoto, T.; Kroger, M.; Kandabarow, A. M.; Park, W.; Barlow, S.; Kim, E. G.; Wielunski, L.; Feldman, L. C.; Bartynski, R. A.; Brédas, J. L.; Marder, S. R.; Kahn, A. *Chem. Mater.* **2010**, *22*, 524.
(122) Lüssem, B.; Riede, M.; Leo, K. *Phys. Status Solidi A* **2013**, *210*, 9.
(123) Li, G.; Shrotriya, V.; Huang, J. S.; Yao, Y.; Moriarty, T.; Emery, K.; Yang, Y. *Nat. Mater.* **2005**, *4*, 864.
(124) O'Regan, B. C.; Lenzmann, F. *J. Phys. Chem. B* **2004**, *108*, 4342.
(125) Barnes, P. R. F.; Miettunen, K.; Li, X. E.; Anderson, A. Y.; Bessho, T.; Gratzel, M.; O'Regan, B. C. *Adv. Mater.* **2013**, *25*, 1881.
(126) Pivrikas, A.; Juska, G.; Mozer, A. J.; Scharber, M.; Arlauskas, K.; Sariciftci, N. S.; Stubb, H.; Osterbacka, R. *Phys. Rev. Lett.* **2005**, *94*, 176806.

(127) Pivrikas, A.; Sariciftci, N. S.; Juska, G.; Osterbacka, R. *Prog. Photovoltaics* **2007**, *15*, 677.
(128) Lyons, B. P.; Clarke, N.; Groves, C. *Energy Environ. Sci.* **2012**, *5*, 7657.
(129) Lyons, B. P.; Clarke, N.; Groves, C. *J. Phys. Chem. C* **2011**, *115*, 22572.
(130) Ratcliff, E. L.; Zacher, B.; Armstrong, N. R. *J. Phys. Chem. Lett.* **2011**, *2*, 1337.
(131) Steirer, K. X.; Ndione, P. F.; Widjonarko, N. E.; Lloyd, M. T.; Meyer, J.; Ratcliff, E. L.; Kahn, A.; Armstrong, N. R.; Curtis, C. J.; Ginley, D. S.; Berry, J. J.; Olson, D. C. *Adv. Energy Mater.* **2011**, *1*, 813.